HHS Public Access

Author manuscript

Nat Cell Biol. Author manuscript; available in PMC 2023 October 31.

Published in final edited form as:

Nat Cell Biol. 2023 July ; 25(7): 950–962. doi:10.1038/s41556-023-01170-4.

Prolonged hypoxia alleviates prolyl hydroxylation-mediated suppression of RIPK1 to promote necroptosis and inflammation

Tao Zhang[1,19], **Daichao Xu**[2,3,19,✉], **Jianping Liu**[4,19], **Min Wang**[1,5,19], **Li-Juan Duan**[6], **Min Liu**[7], **Huyan Meng**[8,9], **Yuan Zhuang**[10], **Huibing Wang**[3], **Yingnan Wang**[1], **Mingming Lv**[1,11], **Zhengyi Zhang**[1], **Jia Hu**[1], **Linyu Shi**[2], **Rui Guo**[2], **Xingxing Xie**[2], **Hui Liu**[1], **Emily Erickson**[1], **Yaru Wang**[4], **Wenyu Yu**[12], **Fabin Dang**[1], **Dongxian Guan**[13], **Cong Jiang**[1], **Xiaoming Dai**[1], **Hiroyuki Inuzuka**[1], **Peiqiang Yan**[1], **Jingchao Wang**[1], **Mrigya Babuta**[10], **Gewei Lian**[14], **Zhenbo Tu**[1], **Ji Miao**[13], **Gyongyi Szabo**[10], **Guo-Hua Fong**[6], **Antoine E. Karnoub**[1,15,16], **Yu-Ru Lee**[17], **Lifeng Pan**[4], **William G. Kaelin Jr.**[12,18], **Junying Yuan**[2,3,✉], **Wenyi Wei**[1,✉]

[1]Department of Pathology and Cancer Center, Beth Israel Deaconess Medical Center, Harvard Medical School, Boston, MA, USA.

[2]Interdisciplinary Center of Biology and Chemistry, Shanghai Institute of Organic Chemistry, Chinese Academy of Sciences, Shanghai, China.

[3]Department of Cell Biology, Harvard Medical School, Boston, MA, USA.

[4]State Key Laboratory of Bioorganic and Natural Products Chemistry, Center for Excellence in Molecular Synthesis, Shanghai Institute of Organic Chemistry, University of Chinese Academy of Sciences, Chinese Academy of Sciences, Shanghai, China.

[5]Department of Biliary-Pancreatic Surgery, Affiliated Tongji Hospital, Tongji Medical College, Huazhong University of Science and Technology, Wuhan, China.

[6]Center for Vascular Biology, Department of Cell Biology, University of Connecticut Health Center, Farmington, CT, USA.

✉**Correspondence and requests for materials** should be addressed to Daichao Xu, Junying Yuan or Wenyi Wei. xudaichao@sioc.ac.cn; Junying_yuan@sioc.ac.cn; wwei2@bidmc.harvard.edu.

Author contributions

T.Z. was the key contributor in designing and conducting the majority of the experiments. T.Z., J.Y. and W.W. conceived of and directed the project and wrote the manuscript. D.X., J.L. and M.W. conducted the key experiments. L.-J.D., M. Liu, H.M., Y.Z., H.W., Yaru Wang, M. Lv, Z.Z., J.H., R.G., X.X., H.L., E.E., Yingnan Wang, W.Y., F.D., D.G., C.J., X.D., H.I., P.Y., J.W., M.B., G.L. and Z.T. conducted some of the experiments. J.M., G.S., G.-H.F., L.P., A.E.K., Y.-R.L. and W.G.K. edited the manuscript. L.S. directed the *Ripk1*^{P196A} knock-in mouse model study. T.Z., Y.Z. and G.S. evaluated the liver sections from the different mice.

Competing interests

W.W. is a co-founder and consultant for Rekindle Therapeutics. G.S. is paid consultant for Cyta Therapeutics, DURECT, Evive, Merck, Pfizer, Surrozen, Terra Firma, Pandion Therapeutics, Labcorp, Glympse Bio, Satellite Bio and Zomagen. The remaining authors declare no competing interests.

Additional information

Extended data is available for this paper at https://doi.org/10.1038/s41556-023-01170-4.

Supplementary information The online version contains supplementary material available at https://doi.org/10.1038/s41556-023-01170-4.

Peer review information *Nature Cell Biology* thanks Holger Eltzschig and the other, anonymous, reviewer(s) for their contribution to the peer review of this work.

Reporting summary

Further information on research design is available in the Nature Portfolio Reporting Summary linked to this article.

[7]Transfusion Medicine, Boston Children's Hospital and Harvard Medical School, Boston, MA, USA.

[8]F.M. Kirby Neurobiology Center, Boston Children's Hospital, Boston, MA, USA.

[9]Department of Neurology, Harvard Medical School, Boston, MA, USA.

[10]Department of Medicine, Beth Israel Deaconess Medical Center, Harvard Medical School, Boston, MA, USA.

[11]Department of Oral and Maxillofacial-Head and Neck Oncology, Shanghai Ninth People's Hospital, College of Stomatology, Shanghai Jiao Tong University School of Medicine, Shanghai Key Laboratory of Stomatology and Shanghai Research Institute of Stomatology, National Clinical Research Center for Oral Diseases, Shanghai, China.

[12]Department of Medical Oncology, Dana-Farber Cancer Institute and Brigham and Women's Hospital, Harvard Medical School, Boston, MA, USA.

[13]Division of Endocrinology, Boston Children's Hospital, Harvard Medical School, Boston, MA, USA.

[14]Department of Neurology, Beth Israel Deaconess Medical Center, Harvard Medical School, Boston, MA, USA.

[15]Harvard Stem Cell Institute, Cambridge, MA, USA.

[16]Broad Institute of MIT and Harvard, Cambridge, MA, USA.

[17]Institute of Biomedical Sciences, Academia Sinica, Taipei, Taiwan.

[18]Howard Hughes Medical Institute, Chevy Chase, MD, USA.

[19]These authors contributed equally: Tao Zhang, Daichao Xu, Jianping Liu, Min Wang.

Abstract

The prolyl hydroxylation of hypoxia-inducible factor 1α (HIF-1α) mediated by the EGLN–pVHL pathway represents a classic signalling mechanism that mediates cellular adaptation under hypoxia. Here we identify RIPK1, a known regulator of cell death mediated by tumour necrosis factor receptor 1 (TNFR1), as a target of EGLN1–pVHL. Prolyl hydroxylation of RIPK1 mediated by EGLN1 promotes the binding of RIPK1 with pVHL to suppress its activation under normoxic conditions. Prolonged hypoxia promotes the activation of RIPK1 kinase by modulating its proline hydroxylation, independent of the TNFα–TNFR1 pathway. As such, inhibiting proline hydroxylation of RIPK1 promotes RIPK1 activation to trigger cell death and inflammation. Hepatocyte-specific *Vhl* deficiency promoted RIPK1-dependent apoptosis to mediate liver pathology. Our findings illustrate a key role of the EGLN–pVHL pathway in suppressing RIPK1 activation under normoxic conditions to promote cell survival and a model by which hypoxia promotes RIPK1 activation through modulating its proline hydroxylation to mediate cell death and inflammation in human diseases, independent of TNFR1.

Hypoxia—a condition induced by a decrease in oxygen availability in tissue or organs—is involved in a multitude of human diseases, including ischaemia of the brain, heart,

liver and kidney[1,2]. Under normoxic conditions, Egl nine homologs (EGLNs) are prolyl hydroxylases (PHDs) that mediate prolyl hydroxylation of hypoxia-inducible factor-1α (HIF-1α), which is recognized by the von Hippel Lindau (VHL) tumour suppressor protein to earmark HIF-1α for proteasomal degradation. Under hypoxic conditions, when the prolyl hydroxylation by EGLNs is inactivated, HIF-1α escapes proteasomal degradation and accumulates in the cells to promote adaptation and cell survival. However, with extensive hypoxic stress, cells would activate the cell death mechanism and die. The molecular regulatory mechanism that links the EGLN–pVHL axis to hypoxia-mediated cell death remains unclear.

Receptor-interacting protein kinase 1 (RIPK1), a critical regulator of cell death and inflammation, is implicated in a multitude of human inflammatory and degenerative diseases[3,4]. Activation of RIPK1 kinase may mediate necroptosis or RIPK1-dependent apoptosis (RDA) upon stimulation of tumour necrosis factor receptor 1 (TNFR1) by tumour necrosis factor α (TNFα), which has remained as the best-characterized model by which RIPK1 is activated[5]. Downstream of TNFR1, activated RIPK1 interacts with RIPK3, which in turn mediates the phosphorylation of mixed lineage kinase domain like pseudokinase (MLKL) to execute necroptosis[6,7]. Alternatively, activated RIPK1 can interact with FAS-associated death domain protein (FADD) and caspase-8 to mediate RDA[4,8]. Inhibition of RIPK1 kinase is highly effective in protecting against hypoxic damage in various organs and tissues[9–13]. The pan-hydroxylase inhibitor dimethyloxalylglycine has previously been shown to induce RIPK1 activation and caspase-independent cell death in monocytes[14]. However, it remains elusive how RIPK1 may be activated under hypoxic conditions.

In this Article, we investigate the molecular mechanism by which hypoxia promotes cell death. We identify that RIPK1 is a prolyl hydroxylation substrate of EGLN1. Under normoxic conditions, EGLN1-mediated prolyl hydroxylation of RIPK1 leads to recognition and suppression of RIPK1 activation by pVHL. Inactivation of prolyl hydroxylation by prolonged hypoxia promotes the activation of RIPK1 and RIPK1-mediated cell death.

Results

Hypoxia promotes RIPK1-driven necroptosis and inflammation

To investigate whether hypoxia can induce RIPK1-dependent necroptosis, we exposed cells to severe hypoxia (1% O_2) for different durations. Exposure to 1% O_2 for 48 h killed wild-type (WT) mouse embryonic fibroblasts (MEFs), whereas most MEFs homozygous for *Ripk1*^{D138N} (a knock-in allele causing the substitution of Asp with Asn at residue 138 in the protein it encodes, killing the activity of RIPK1 kinase)[15] survived. Inhibition of RIPK1 protected against cell death induced by hypoxia (Fig. 1a and Extended Data Fig. 1a). Moreover, hypoxia increased the levels of phospho-RIPK1-Ser166 (p-RIPK1-S166), a hallmark of RIPK1 activity[16,17] (Fig. 1b,c and Extended Data Fig. 1b,c). To further characterize whether hypoxia-induced necroptosis depends on RIPK1–RIPK3–MLKL, we challenged WT and *Ripk3* knockout or *Mlkl* knockout MEFs with hypoxia. Deletion of either *Ripk3* or *Mlkl* strongly inhibited cell death induced by hypoxia (Fig. 1d,e and Extended Data Fig. 1d). We challenged several different cell lines, including L929, HT-29, Jurkat, THP-1 and human skin fibroblast cells under hypoxic conditions. Interestingly,

hypoxia could trigger all of these different cell lines to undergo cell death that was decreased by treatment with the RIPK1 inhibitor necrostatin-1s (Nec-1s)[9]. These results suggest the existence of a common mechanism for hypoxia-induced RIPK1 activation and cell death (Extended Data Fig. 1e–p).

Increased insolubility is another hallmark of activated RIPK1–RIPK3–MLKL[17]. In WT MEFs exposed to hypoxia, the levels of mild detergent (NP-40)-soluble RIPK1, RIPK3 and MLKL were decreased and those of 6 M urea-soluble/NP-40-insoluble fractions were increased (Fig. 1c)[15]. Furthermore, we found that genetic ablation of *RIPK1* abolished hypoxia-induced cell death (Extended Data Fig. 1j) and ameliorated the elevation of RIPK3–MLKL activity, as demonstrated by p-RIPK3(T231/S232) or solubility changes in RIPK3–MLKL (Extended Data Figs. 1k,l). Inhibition of caspases is crucial for promoting the interaction of RIPK1 and RIPK3 to activate necroptosis in the TNFα signalling pathway[18–20]. Interestingly, hypoxia induced the interaction of RIPK1 and RIPK3 in WT MEFs without caspase inhibition at 24 h (Fig. 1f).

To delineate the oxygen sensitivity of RIPK1–RIPK3 activity, we exposed cells to different concentrations of oxygen. Only severe hypoxia (1% O_2) could increase the levels of p-RIPK1-S166 and p-MLKL-S345, whereas mild or moderate hypoxia (3% O_2) mainly induced HIF-1α without the activation of RIPK1 and induction of necroptosis (Fig. 1g and Extended Data Fig. 1q–s), indicating that the activity of RIPK1 is regulated in an oxygen-dependent manner. Importantly, *Tnfr1* knockout MEFs died at a comparable level to that of WT MEFs after exposure to 1% O_2, strongly suggesting that hypoxia promoted the activation of RIPK1 independent of the TNFα–TNFR1 pathway (Extended Data Fig. 1t). A previous study[14] showed that the hypoxia mimetic agent dimethyloxalylglycine caused a decrease in cellular inhibitor of apoptosis protein-1 (cIAP1) expression. Nevertheless, since cIAP1/2-mediated ubiquitination suppresses RIPK1 kinase activation and cIAP1/2 inhibition triggers RIPK1-dependent cell death[21], we considered whether decreased cIAP expression might be involved in hypoxia-mediated RIPK1 activation and cell death. However, deletion of *cIAPs* did not affect hypoxia-induced cell death or the activation of RIPK1, which occurred at a comparable level in both control and *cIAPs* knockout MEFs (Extended Data Fig. 1u–w). Furthermore, knockout of *Hif1β*, the HIF-1α heterodimer binding partner required for its transcriptional activity, did not affect hypoxia-induced cell death and activation of RIPK1, suggesting that HIF-1 does not directly inhibit this pathway (Extended Data Fig. 1x–z).

To characterize the role of RIPK1 and TNF in hypoxia in vivo, we subjected WT, *Ripk1*$^{D138N/D138N}$ (ref. 15) and *Tnfr1/2* double knockout mice to 6% O_2 hypoxia[22] or 11% O_2 hypoxia[23] for 72 h (Fig. 1h,i and Extended Data Fig. 2a). Hypoxia with 6% O_2, but not 11% O_2, substantially increased the number of cells with p-RIPK1-S166 in the liver and brain of WT and *Tnfr1/2* double knockout mice, but not in *Ripk1*$^{D138N/D138N}$ mice (Fig. 1h,i and Extended Data Fig. 2b,c). Next, we examined the downstream inflammatory responses of RIPK1 kinase in response to both 6 and 11% O_2 hypoxia in vivo. Only severe hypoxia (6% O_2) could induce the expression of cytokines both in the liver and the brain. Inhibition of RIPK1 dramatically decreased the production of pro-inflammatory cytokines (Fig. 1j and Extended Data Fig. 2d). Treatment with 6% hypoxia induced cell death (increasing

the numbers of terminal deoxynucleotidyl transferase dUTP nick end labelling-positive ($TUNEL^+$) cells) and liver damage (Extended Data Fig. 2e–g).

Hypoxia promotes major infiltration of myeloid cells and tissue remodelling in the lung[24–26]. Interestingly, hypoxia induced RIPK1 activity in the lungs from the mice exposed to hypoxia, and genetic inhibition of *Ripk1* decreased infiltration of myeloid cells in the lungs caused by hypoxia (Extended Data Fig. 2h,i). These results suggest that hypoxia can promote the activation of immune cells by activating RIPK1 kinase.

Inhibition of EGLN1 activates RIPK1 to trigger cell death and inflammation

Hypoxia-induced activation of HIFs is mediated primarily via the inhibition of PHDs[27]. Hence, we next explored whether these PHDs could modify RIPK1. RIPK1 interacted with PHDs, and the binding between RIPK1 and PHD2 (also called EGLN1) was comparatively stronger than that between RIPK1 and PHD1 (EGLN2) or PHD3 (EGLN3) (Fig. 2a). We also mapped the domains of EGLN1 and RIPK1 that interact with each other and found that EGLN1 bound preferentially with the kinase domain of RIPK1 (Extended Data Fig. 3a), while RIPK1 bound primarily with the amino terminus of EGLN1 (Extended Data Fig. 3b). Overexpression of RIPK1 in 293T cells led to its auto-activation, as marked by p-RIPK1-S166 (ref. 16). Ectopic expression of EGLN1, but not EGLN2 or EGLN3, suppressed RIPK1 activation in this 293T cell model (Fig. 2b). This result suggests that EGLN1 may directly suppress the activation of RIPK1.

Deletion of *Egln1* or EGLN inhibition with the EGLN inhibitor FG-4592 (refs. 23,28–30) could sensitize cell death induced by hypoxia (Fig. 2c,d). We examined possible functional relationships between EGLN1 and RIPK1 using additional EGLN inhibitors (that is, cobalt chloride ($CoCl_2$)[31] and dimethyloxaloylglycine deferoxamine (DFO)[32]). Strikingly, cells treated with these inhibitors alone showed the hallmarks of RIPK1, RIPK3 and MLKL activation (Extended Data Fig. 3c–f). Treatment with FG-4592 at a relatively high concentration activated RIPK1 and induced necroptosis in multiple cell lines, such as HT-29 and MEFs (Fig. 2e–g and Extended Data Fig. 3g–j). To further investigate the involvement of necroptosis in FG-4592 treatment-induced cell death, we treated WT and *Mlkl* knockout cells with FG-4592 and found that deletion of *Mlkl* decreased cell death induced by FG-4592 treatment (Extended Data Figs. 3k,l). Moreover, we found that inhibition of MLKL by necrosulfonamide can also suppress cell death induced by treatment with FG-4592 in HT-29 cells (Extended Data Fig. 3m). Thus, inhibition of EGLNs alone can be sufficient to trigger necroptosis. Only high concentrations of $CoCl_2$, DFO and FG-4592 can activate RIPK1 and necroptosis (Fig. 2e,f and Extended Data Fig. 3c,e,g).

To determine the physiological function of *Egln* genes in the regulation of RIPK1 activation in vivo, we conditionally deleted *Egln1* or all three *Egln* genes using mice harbouring *Alb-Cre* and $Egln1^{fl/fl}$::$Egln2^{fl/fl}$::$Egln3^{fl/fl}$ alleles[33]. The efficiency of knockout *Egln1/Egln2/Egln3* and hepatic upregulation of HIF-1α and HIF-2α have been demonstrated previously (Extended Data Fig. 3n)[33]. Hepatic triple deficiency of all three isoforms caused multiple abnormalities, including vascular malformation and increased infiltration of inflammatory cells, indicating the activation of strong inflammation (Fig. 2h). Immunostaining for p-RIPK1-S166 and cleaved caspase-3 (CC3)—a marker for apoptosis—revealed dramatic

RIPK1 activation and extensive cell death in the liver of *Egln* triple knockout mice (Fig. 2i). *Egln1*$^{fl/fl}$::*Egln2*$^{fl/fl}$::*Egln3*$^{fl/fl}$::*Alb-Cre* mice also showed elevated levels of serum alanine aminotransferase (ALT) and aspartate aminotransferase (AST) but not bilirubin (Extended Data Fig. 3o) and hepatic fibrosis (Extended Data Fig. 3p). The pro-inflammatory cytokine S100A8 was also induced in the liver of *Egln* triple knockout mice (Extended Data Fig. 3q). The numbers of activated macrophages and neutrophils (CD11b and Ly-6G) were dramatically increased compared with in control mice (Extended Data Fig. 3r). With double immunostaining for CC3 or p-RIPK1-S166 with different cell type markers, we found that almost all of the CC3- and p-RIPK1-positive cells were hepatocytes (Extended Data Figs. 4a–h).

To investigate whether the pharmacological inhibition of EGLN proteins could recapitulate the phenotype caused by *Egln* genetic deficiencies in vivo, we treated both WT and RIPK1 kinase-dead (*Ripk1*^{D138N}) mice with the EGLN-specific inhibitor FG-4592 (refs. 23,28–30) at different doses (25, 50 and 250 mg kg^{-1} body weight) (Extended Data Fig. 4i). FG-4592 at 25 or 50 mg kg^{-1} body weight did not induce RIPK1 activation or cell death (Extended Data Fig. 4j). However, FG-4592 at 250 mg kg^{-1} body weight caused substantial liver damage, with a large number of TUNEL^{+} cells and increased p-RIPK1-S166 by immunostaining[34] in the liver (Fig. 2j and Extended Data Fig. 4j) and elevated levels of pro-inflammatory cytokines such as those encoded by *Il6* and *C-C motif chemokine ligand 2 (Ccl2)*, compared with in control mice (Fig. 2k). Inhibition of RIPK1 with homozygous *Ripk1*^{D138N} mutation or Nec-1s dramatically decreased cell death and the production of pro-inflammatory cytokines, thereby revealing a pivotal role of RIPK1 activity in this process (Fig. 2j,k and Extended Data Fig. 4j–l).

EGLN1 mediates hydroxylation of RIPK1 at multiple Pro residues

Next, we investigated the mechanism by which EGLN1 directly inhibits RIPK1 kinase. We performed a mass spectrometry analysis to determine the proline site(s) on RIPK1 that can be hydroxylated by EGLN1. Multiple proline residues of RIPK1 were modified by prolyl hydroxylation in cells, including 11 Pro residues (that is, Pro51, Pro195, Pro247, Pro276, Pro353, Pro361, Pro366, Pro478, Pro481, Pro492 and Pro498) (Extended Data Fig. 5a–c). Moreover, the proline hydroxylation status of RIPK1 could be detected with a pan-hydroxylation antibody, which could be blocked by the EGLN inhibitor $CoCl_2$ (Extended Data Fig. 5d)[31].

Next, we focused our analysis on the hydroxylation of Pro195 in human RIPK1 (Pro196 of murine RIPK1), which is critical for the activation of RIPK1 (refs. 16,35) (Extended Data Fig. 5a–c). Using a reconstituted in vitro hydroxylation assay[36], we found that recombinant EGLN1 hydroxylated a synthetic RIPK1 peptide containing Pro195 (Fig. 3a,b and Extended Data Fig. 5e,f). These data identified Pro195 as a hydroxylation site mediated by EGLN1. To further determine that Pro195 of RIPK1 is modified in cells, we generated and validated an antibody that could specifically recognize the RIPK1 Pro195 hydroxylation event in cells expressing WT RIPK1, but not the mutant protein with Pro substituted for Ala at amino acid residue 195 (RIPK1-P195A) (Extended Data Fig. 5g). Pro195 hydroxylation of RIPK1, which does not lead to mislocalization of RIPK1 (Extended Data Fig. 5h), was inhibited by

Egln1 deficiency, FG-4592 and hypoxia (Fig. 3c–f and Extended Data Fig. 5i). Furthermore, FG-4592 treatment can also reduce the proline hydroxylation of RIPK1 at Pro196 in vivo (Fig. 3g).

Since Pro195 is localized in the activation loop critical for the activation of RIPK1 (refs. 16,35), we considered the possibility that Pro195 hydroxylation of RIPK1 by EGLN1 regulates RIPK1 activity. Overexpression of the human RIPK1-P195A mutant led to higher levels of p-RIPK1-S166 compared with the WT, and both were effectively inhibited by Nec-1s (Fig. 4a). We performed in vitro kinase assays and found that the RIPK1-P195A mutant has higher activity than WT RIPK1 (Fig. 4b), suggesting that Pro195 hydroxylation negatively regulates RIPK1 activity. Only treatment with high doses of FG-4592 led to a decrease in the hydroxylation of RIPK1 and corresponding increases in RIPK1 activity and cell death, which may have been due to the presence of extensive prolyl hydroxylation modifications in RIPK1 (Fig. 3f,g and Extended Data Fig. 5a,b).

RIPK1-P196A alteration promotes RIPK1 activation and cell death in mice

Pro196 in murine RIPK1 corresponds to Pro195 in human RIPK1 (Extended Data Fig. 5c). We generated *Ripk1*$^{P196A/P196A}$ knock-in mutant mice by mutating the conserved hydroxyproline (P) at position 196 to alanine (P196A) using CRISPR–Cas9 technology (Extended Data Fig. 6a–c). While *Ripk1*$^{P196A/P196A}$ mutant mice were born with normal Mendelian ratios (Extended Data Fig. 6d), their growth was severely retarded and infertile (Fig. 4c and Extended Data Fig. 6e–g). We performed histological analysis and TUNEL assays on sections from the intestines of WT and *Ripk1*$^{P196A/P196A}$ mutant mice. *Ripk1*$^{P196A/P196A}$ mutant mice showed intestinal degeneration with a large number of TUNEL^{+} cells (Fig. 4d). We also detected increased p-RIPK1-S166 by immunostaining in the intestines of *Ripk1*$^{P196A/P196A}$ mice compared with WT counterpart mice (Fig. 4d). Adult *Ripk1*$^{P196A/P196A}$ mutant mice showed elevated levels of pro-inflammatory cytokines and chemokines, such as TNFα, interleukin 1α (IL-1α), IL-1β, CCL2 and IL-6, in serum samples, many of which are known to be regulated by RIPK1 (Fig. 4e)[37]. A strong inflammatory response was also found to be activated in the intestines and liver of adult *Ripk1*$^{P196A/P196A}$ mice (Extended Data Fig. 6h,i). Mild cell death and liver damage were found in adult *Ripk1*$^{P196A/P196A}$ mice (Extended Data Fig. 7a–d). To demonstrate the role of RIPK1 activation in the pathology caused by RIPK1-P196A mutation, we treated WT and *Ripk1*$^{P196A/P196A}$ mice with the RIPK1 inhibitor Nec-1s. Inhibition of RIPK1 with Nec-1s decreased cell death and inflammation in *Ripk1*$^{P196A/P196A}$ mice (Fig. 4f and Extended Data Fig. 7e). We also treated WT and *Ripk1*$^{P196A/P196A}$ mice with the EGLN inhibitor FG-4592 and found that at a dose of 25 mg kg^{-1} body weight it can only induce the HIF pathway, without induction of RIPK1 activation and cell death (Extended Data Fig. 7f–h). In keeping with the hypothesis that additional hydroxylation sites besides Pro196 probably exist that can also contribute to RIPK1 regulation, we found that treatment with FG-4592 at a dose of 250 mg kg^{-1} body weight can further exacerbate liver damage and inflammation compared with that of *Ripk1*$^{P196A/P196A}$ mice without treatment (Extended Data Fig. 7i–l).

pVHL suppresses RIPK1 kinase activity through direct binding

Given that the pVHL tumour suppressor is an authentic reader of Pro hydroxylation events in cells[38–40], we went on to investigate whether RIPK1 might interact with pVHL and whether Pro195 hydroxylation in RIPK1 might affect this interaction. Ectopically expressed pVHL bound with endogenous RIPK1 and the interaction was decreased in response to hypoxia (Fig. 5a), suggesting that the binding between pVHL and RIPK1 was probably proline hydroxylation dependent. Inhibiting RIPK1 hydroxylation with either hypoxia (Fig. 5a), *EGLN1* knockdown (Fig. 5b) or the EGLN inhibitor DFO (Extended Data Fig. 8a,b) markedly decreased pVHL interaction with RIPK1 in cells. Consistently, we further found that altering Pro195, but not Pro51, Pro279 or Pro195, in RIPK1 decreased the interaction between pVHL and RIPK1 in cells, further supporting Pro195 as a major hydroxylation site in RIPK1 that mediates its recognition by pVHL (Extended Data Fig. 8c).

Next, we explored whether pVHL can affect the activity of RIPK1 through its physical interaction with RIPK1. Reintroducing pVHL in *VHL*-deficient renal carcinoma cells decreased the levels of p-RIPK1-S166 induced by treatment with a combination of TNFα, cycloheximide and zVAD-fmk (TCZ) (Fig. 5c). Furthermore, the expression of pVHL decreased the activation of ectopically expressed RIPK1 in a dose-dependent manner (Extended Data Fig. 8d), suggesting that pVHL can directly suppress RIPK1 activation. Cre[41]-mediated deletion of *Vhl* in MEFs sensitized cells to hypoxia-induced necroptosis, which could be decreased with the administration of Nec-1s (Fig. 5d). Moreover, ectopic overexpression of pVHL or EGLN1 blocked the activation of WT RIPK1, but not that of RIPK1-P195A (Fig. 5e), demonstrating the importance of Pro195 hydroxylation in RIPK1. We performed in vitro kinase assays and found that recombinant pVHL could dramatically inhibit induction of the kinase activity of WT RIPK1 but not mutant RIPK1-P195A (Fig. 5f and Extended Data Fig. 8e,f). Taken together, these data suggest that pVHL suppresses RIPK1 kinase activity by directly binding to the Pro195-hydroxylated activation loop of RIPK1.

Co-crystal structure of pVHL bound with hydroxylated RIPK1 peptide

We further characterized the direct binding between pVHL and RIPK1 in vitro. Notably, the activation loop (amino acid residues 156–200) of RIPK1 contains an $_{190}$LYYMAP$_{195}$ motif similar to the LxxLAP motif in HIF-1α (Extended Data Fig. 8g), which is a well-defined substrate of PHDs and a binding partner of pVHL[38,39]. Direct binding between pVHL (in complex with elongin C and elongin B (VCB)) and the RIPK1 peptide depends on hydroxylation of the Pro195 residue and can be readily detected in peptide pull-down assays (Fig. 6a and Extended Data Fig. 8h,i). The binding affinity (dissociation constant (K_d)) of RIPK1 peptide for pVHL was 5.9 ± 1.1 μM, as determined by fluorescence polarization assay (Fig. 6b and Extended Data Fig. 8j), which is comparable to that of the HIF-1α peptide for pVHL (1.0 ± 0.1 μM) (Fig. 6c).

To reveal the critical residues in pVHL that recognize hydroxylated RIPK1, we solved the structure of VCB proteins in complex with a RIPK1 peptide (residues 189–203, with Pro195 being hydroxylated) at a resolution of 2.8 Å using X-ray crystallography (Fig. 6d,e, Extended Data Fig. 8k and Supplementary Table 1). In the RIPK1 peptide, only residues

190–199 (LYYMAPEHLN) could be traced in the electron density map. The RIPK1 peptide binds to one side of the β-domain of pVHL in an extended conformation (Fig. 6d,e). The same binding pocket present in pVHL binds to the LxxMA(Hyp) motif in RIPK1 and the LxxLA(Hyp) motif in HIF-1α, where Hyp represents hydroxylation on the proline residue (Extended Data Fig. 8l,m)[42,43]. Pro195—the main hydroxylation site in the RIPK1 activation loop—is also a direct binding site for recruiting VHL to suppress RIPK1 activity (Figs. 4a,b, 5e,f and Fig. 6e,f).

Since Pro195 is in the activation loop whose conformation controls the activity of RIPK1 kinase[16,35], direct binding of VHL to hydroxyl proline-195 (HyPro195) of RIPK1 may inhibit its kinase activity by hampering the activation loop to adopt an active conformation (Fig. 6f). We found good congruence between the residues in the hydroxyl-proline binding pocket of pVHL that bind to both RIPK1 and HIF-1α (Fig. 6d.e and Extended Data Fig. 8k–m). Altering the key residues of the hydroxyl-proline recognition pocket in pVHL that bind to HIF-1α[42,43], including W117, W88, Y98 and S111, also abolished pVHL interaction with RIPK1 in cells (Fig. 6g). Furthermore, only the WT form of VHL (but not mutant forms) could block the activation of overexpressed RIPK1 in 293T cells (Extended Data Fig. 8n).

The backbone root mean square deviation between the RIPK1 and HIF-1α complexes is 0.34 Å. In the RIPK1 peptide complex, in addition to the snug fit between the central residue HyPro195 and VHL, some peripheral residues also contribute to the specificity of binding. Both hydrophobic and polar interaction can be found in the peripheral region (Fig. 6e). Compared with the HIF-1α peptide, the RIPK1 peptide lacks a long acidic tail with which to form additional polar interaction with VHL (Extended Data Fig. 8m). This difference explains why VHL has a lower affinity to RIPK1 than to HIF-1α. Further competition binding assay found that the proline-hydroxylated HIF-1α peptide, but not its non-hydroxylated version, can compete with RIPK1 peptide for binding with VHL in vitro (Fig. 6h,i).

The protein abundances of RIPK1 and cIAP1 were not affected by depleting *VHL* (Extended Data Fig. 8o,p). Depletion of endogenous *Cul2*, which is required for VHL-dependent ubiquitination and leads to the degradation of HIFα, did not change the protein levels of RIPK1 (Extended Data Fig. 8q). Moreover, pVHL could not promote ubiquitination of RIPK1 (Extended Data Fig. 8r–t). We exposed *Vhl* knockout MEFs reconstituted with WT or catalytically inactive VHL to hypoxia. Both WT and catalytically inactive VHL (a truncated mutant VHL; amino acids 1–154)[44] could suppress RIPK1 activation and cell death in response to hypoxia (Extended Data Fig. 8u,v). Taken together, all of these data suggest that VHL suppresses RIPK1 activation and cell death in an E3 ligase-independent manner (Extended Data Fig. 8p–v).

To examine the potential contribution of RIPK1 prolyl hydroxylation to the TNFR1 pathway, we treated primary WT MEFs or MEFs bearing the *Ripk1*$^{P196A/P196A}$ mutation with a combination of TNFα, SM-164 and zVAD.fmk (TSZ) or a combination of TNFα and SM-164. MEFs with the *Ripk1*$^{P196A/P196A}$ mutation exhibited a slightly increased sensitivity to RDA induced by combined treatment with TNFα and SM-164 and necroptosis

induced by TSZ compared with WT MEFs (Extended Data Fig. 9a,b). In the RIPK1-P196A mutant, the levels of p-RIPK1-S166 were markedly increased in the presence of TSZ or a combination of TNFα and SM-164, and both the increased cell death and RIPK1 activation were inhibited upon treatment with the RIPK1 inhibitor Nec-1s[9] (Extended Data Fig. 9c–e).

Next, we explored whether deletion of *Egln1* or treatment with EGLN inhibitors could also sensitize cells to cell death upon stimulation of TNFR1 by TNFα. Consistent with the binding data (Fig. 2a), *Egln1*$^{-/-}$ MEFs (but not *Egln2*$^{-/-}$ or *Egln3*$^{-/-}$ MEFs) were much more sensitive to necroptosis induced by TCZ or TSZ (Extended Data Fig. 9f–i) and RDA induced by combined treatment with TNFα and 5z-7-oxozeaenol (5z7) compared with WT MEFs (Extended Data Fig. 9j,k). Importantly, FG-4592 treatment could sensitize cells to cell death induced by TSZ treatment (Extended Data Fig. 9i). Furthermore, knockout of *Egln1* markedly increased the levels of p-RIPK1-S166 in the presence of TCZ (Extended Data Fig. 9g). The RIPK1 inhibitor Nec-1s blocked the cell death of *Egln1*$^{-/-}$ MEFs induced by either TSZ or a combination of TNFα and 5z7 (Extended Data Fig. 9f–h,j,k). Moreover, deletion of *Vhl* in MEFs sensitized cells to TSZ-induced necroptosis (Extended Data Fig. 9l). VHL suppressed the RDA induced by combined treatment with TNFα, 5z7 and SM-164 in 786-o cells—a process that could be blocked by Nec-1s (Extended Data Fig. 9m). These results suggest that *Vhl* deficiency sensitizes cells to necroptosis and RDA.

Inhibition of RIPK1 suppresses liver damage induced by *Vhl* deletion

Conditional inactivation of *Vhl* in hepatocytes (*Vhl* liver conditional knockout (LKO)) led to severe steatohepatitis, decreased body weight and premature death (Extended Data Fig. 10a–d), which was attributable to dysregulated lipid metabolism due to elevated HIF-2α, as the phenotype was largely rescued by *Hif2a* knockout[45]. We co-stained TUNEL and the hepatocyte cell maker hepatocyte nuclear factor 4α (HNF4α) and found that the TUNEL-positive cells were hepatocytes (Extended data Fig. 10e). In support of the role for RIPK1 in mediating the death of hepatocytes induced by *Vhl* deficiency, we detected p-RIPK1-S166 and cell death (TUNEL^{+}) in the livers of *Vhl* LKO mice, which was inhibited upon inactivation of RIPK1 in *Vhl* LKO; *Ripk1*$^{D138N/D138N}$ mice (Fig. 7a,b and Extended Data Fig. 10f). The known defects in lipid metabolism induced by *Vhl* LKO, as indicated by abnormal Oil Red O staining[45], were not rescued by *Ripk1*^{D138N} mutation, suggesting that inhibition of RIPK1 has no effect on dysregulated hepatocytic lipid metabolism induced by hepatocytic *Vhl* deficiency (Extended Data Fig. 10g). Interestingly, inhibition of RIPK1 in *Vhl* LKO;*Ripk1*$^{D138N/D138N}$ mice blocked apoptosis, as indicated by CC3 in *Vhl*-deficient livers (Fig. 7c,d and Extended Data Fig. 10h,i). However, inhibition of RIPK1 had no effect on either the messenger RNA or protein levels of HIF and HIF downstream targets, such as *Bnip3*, *Bnip3l* and *Noxa*, which further excluded crosstalk between RIPK1 and canonical adaptive hypoxia pathways (Fig. 7d and Extended Data Fig. 10j). *Vhl* LKO;*Ripk1*$^{D138N/D138N}$ mice also showed decreased levels of ALT and AST compared with *Vhl* LKO mice (Fig. 7e). The spleen and liver weights of *Vhl* LKO;*Ripk1*$^{D138N/D138N}$ mice were largely normalized compared with those of *Vhl* LKO mice (Extended Data Fig. 10k,l). Moreover, inhibition of RIPK1 dramatically decreased the production of pro-inflammatory cytokines (Fig. 7f), the infiltration of macrophages (F4/80^{+}) (Extended Data Fig. 10m) and hepatic fibrosis in *Vhl* LKO mice (Fig. 7g and Extended Data Fig. 10n). Furthermore, *Vhl*

LKO;*Ripk1*$^{D138N/D138N}$ mice had increased weight gain and survived much longer than *Vhl* LKO mice (Fig. 7h and Extended Data Fig. 10o). To further demonstrate the role of PRIK1 in mediating the liver pathology caused by *Vhl* deficiency, We treated *Vhl* LKO mice with Nec-1s. Consistent with genetic inhibition of RIPK1 via *Ripk1*$^{D138N/D38N}$ mutation (Fig. 7a–d,f), we found that treatment with Nec-1s also blocked RIPK1 activation, cell death and inflammation in *Vhl* hepatocyte-specific knockout mice (Extended Data Fig. 10p–r).

As hepatocytes do not express RIPK3 under basal conditions, they are resistant to RIPK3-mediated necroptosis and die exclusively by apoptosis[46,47]. These data demonstrate that RIPK1-dependent apoptosis probably plays a major role in mediating cell death in *Vhl* LKO mice, and suggest that pVHL deficiency-induced severe hepatocyte death is mediated by RDA.

Discussion

Our study reveals a pathway that modulates the activation of RIPK1 and RIPK1-dependent cell death mediated by EGLNs and pVHL under severe hypoxic conditions. Our mass spectrometry analysis demonstrates that up to 11 Pro residues in RIPK1 may be subject to prolyl hydroxylation, whereas HIF-1α is hydroxyl modified only on two Pro residues: Pro402 and Pro564 (refs. 38–40,48). Extensive prolyl hydroxylation of RIPK1 may explain why prolonged severe hypoxia and a high dose of EGLN inhibitor is needed to activate RIPK1 (Fig. 1a–g and Extended Data Fig. 1b–w). While mild hypoxia is sufficient to inactivate the two prolyl hydroxylation sites in HIF-1α, disrupting its binding with pVHL and allowing HIF-1 to escape proteasomal degradation, it is probably insufficient to inactivate the extensive prolyl hydroxylation in RIPK1 to promote its activation. Thus, mild hypoxia leads to the stabilization of HIF-1 to mediate the adaptive response, while only severe hypoxia can activate RIPK1 to promote cell death (Fig. 7i).

Hypoxia is a common feature of many inflammatory diseases[49,50]. Moreover, it can induce inflammation[51] and promote major infiltration of myeloid cells and tissue remodelling in organs such as the lungs[24–26]. In the current study, we found that hypoxia can induce RIPK1 activity in the lungs of mice exposed to hypoxia, and genetic inhibition of RIPK1 decreased myeloid cell infiltration in the lungs under hypoxia (Extended Data Fig. 2h,i). These results suggest that hypoxia can promote the activation of immune cells by induction of RIPK1 kinase activity. Since we found that hypoxia can activate RIPK1 and RIPK1 kinase-dependent inflammation, targeting hypoxia signalling by inhibition of RIPK1 may provide an effective strategy for the treatment of ischaemic and inflammatory diseases characterized by tissue hypoxia.

Online content

Any methods, additional references, Nature Portfolio reporting summaries, source data, extended data, supplementary information, acknowledgements, peer review information; details of author contributions and competing interests; and statements of data and code availability are available at https://doi.org/10.1038/s41556-023-01170-4.

Methods

Our research complies with all of the relevant ethical regulations. The animal experiments performed at the Beth Israel Deaconess Medical Center were in accordance with animal protocol 019–2021, which was approved by the Institutional Animal Care and Use Committee at the Beth Israel Deaconess Medical Center, and in accordance with guidelines established by the National Institutes of Health *Guide for the Care and Use of Laboratory Animals*.

Animals

Albumin-Cre (B6.Cg-*Speer6-ps1*$^{Tg(Alb\text{-}cre)21Mgn}$/J; catalogue number 003574), *Vhl*$^{fl/fl}$ (B6.129S4(C)-*Vhl*^{tm1Jae}/J; catalogue number 012933) and *Tnfrn1/2* knockout (B6.129S-*Tnfrsf1a*^{tm1Imx} *Tnfrsf1b*^{tm1Imx}/J; catalogue number 003243) mice were purchased from The Jackson Laboratory. *Ripk1*^{D138N} mice were used in this study[15]. Mouse lines carrying conditional knockout genes for PHDs (*Egln1*$^{fl/fl}$, *Egln2*$^{fl/fl}$ and *Egln3*$^{fl/fl}$ genotypes) were used[33]. *Vhl*$^{fl/fl}$ mice were crossed with *Albumin-Cre* to generate *Vhl* LKO mice. *Vhl*$^{fl/+}$;*Albumin-Cre*;*Ripk1*$^{D138N/D138N}$ mice were intercrossed to generate *Vhl*$^{fl/fl}$;*Albumin-Cre*;*Ripk1*$^{D138N/D138N}$ mice. The mice used were in the C57BL/6J genetic background. All mice were kept on a 12 h light/12 h dark cycle.

Mouse genotyping

Genomic DNA was extracted from mouse ears. PCR was performed with KAPA Mouse Genotyping Kits (KK5621; KAPA) using the following primers for *Ripk1*^{D138N}: 5′-TACCTTCTAACAAAGCTTTCC-3′ (common), 5′-AATGGAACCACAGCATTGGC3′ (WT) and 5′-CCCTCGAAGAGGTTCACTAG3′ (knockdown). *Albumin-Cre* and *Vhl*$^{fl/fl}$ mouse genotyping was performed according to The Jackson Laboratory instructions. Briefly, *Vhl*$^{fl/fl}$ genotyping was performed using the following PCR primers: 5′- AAGAGCACGCAGCTTAGGAG-3′ (forward) and 5′-TTTCTGAGTCCTGGGGATTG-3′ (reverse). For *Egln1*$^{fl/fl}$ we used 5′-CAAATGGAGATGGAAGATGC-3′ (forward) and 5′- TCAACTCGAGCTGGAAACC-3′ (reverse); for *Egln2*$^{fl/fl}$ we used 5′-TGGGCGCTGCATCACCTGTATCT-3′ (forward) and 5′-ACTGGTGAAGCCTGTAGCCTGTC-3′ (reverse); for *Egln3*$^{fl/fl}$ we used 5′-ATGGCCGCTGTATCACCTGTAT-3′ (forward) and 5′-CCACGTTAACTCTAGAGCCACTGA-3′ (reverse); for *Albumin-Cre* we used 5′-TTGGCCCCTTACCATAACTG-3′ (common), 5′-TGCAAACATCACATGCACAC-3′ (WT) and 5′-GAAGCAGAAGCTTAGGAAGATGG-3′ (mutant); and for the *Tnfrn1/2* knockout we used 5′-GCTACTTCCATTTGTCACGTCC-3′ (mutant), 5′-ATGGGGATACATCCATCAGG-3′ (common) and 5′-GGGGAACATCAGAAACAAGC-3′ (WT). The *Ripk1*$^{P196A/P196A}$ genotyping primers were 5′-TTCACACACACATCTTGGCA-3′ (forward) and 5′-TGGAGGTGGAGGTGGAGATA-3′ (reverse). The *Ripk1*$^{P196A/P196A}$ digestion enzyme used was DraI (R0129S; NEB). Amplicons were analysed by agarose gel electrophoresis.

Generation of *Ripk1*^{P196A} mutant mice

Super-ovulated female C57BL/6 mice (8 weeks old) were mated with C57BL/6 males and the zygotes were collected from the oviducts. Single-stranded oligonucleotides (ssODNs) were synthesized by Sangon. Cas9 messenger RNA (100 ng μl^{-1}), single guide RNA (sgRNA; 50 ng μl^{-1}) and ssODNs (100 ng μl^{-1}) were mixed in M2 medium (Sigma–Aldrich) and injected into the cytoplasm of zygotes using a microinjector (FemtoJet; Eppendorf). The pups were identified by both enzyme digestion and DNA sequencing. The positive mice were mated with WT C57BL/6 mice to produce heterozygous RIPK1-P196A mutant progenies, which were then backcrossed with C57BL/6 mice. The target sequence was 5′-ATTGATGTCATTCAGGTGTT-3′. The sequence of the Pro196A ssODN was 5′-AGAAAGAAGTGAGCAGCACCACTAAGAAGAACAATGGTGGTACCCTTTACTACATGGCAGCCGAACA **TT**T**A**AATGACATCAATGCAAAGCCCACGGAGAAGTCGGACGTGTACAGCTTTGGCATTGTCCT-3′, where the synonymous mutation is shown in bold and the point mutation is underlined.

Administration of FG-4592 in vivo

FG-4592 was dissolved in 5% dextrose and administered intraperitoneally as seven doses (25 mg kg^{-1} body weight) over 7 d or two doses (50 and 250 mg kg^{-1} body weight) over 2 d to WT, *Ripk1*^{D138N} or *Ripk1*^{P196A} mice. The mice were sacrificed and tissues and blood were collected for further analysis.

Administration of Nec-1s in vivo

Custom synthesized Nec-1s was first dissolved in dimethyl sulfoxide (50% wt/vol), transferred into 35% polyethylene glycol solution and suspended in water containing 2% sucrose. The mice were provided with vehicle control or Nec-1s as drinking water ad libitum. Each mouse drank ~5–10 ml d^{-1} vehicle or Nec-1s containing water (Nec-1s = 2.5–5 mg d^{-1}).

Cell lines and cell culture

The following cell lines were used: HEK293T cells (CRL-3216; American Type Culture Collection (ATCC)), L929 cells (CCL-1; ATCC) and MEFs in Dulbecco's modified Eagle medium (Gibco) with 10% foetal bovine serum (FBS; Gibco) and 1% penicillin/streptomycin; THP-1 and Jurkat cells (TIB-152; ATCC) in RPMI-1640 (Life Technologies) with 10% FBS and 1% penicillin/streptomycin; and HT-29 cells (HTB-38; ATCC) in McCoy's 5A (Gibco). Hypoxic culture conditions were achieved with an O_2/CO_2 incubator containing a gas mixture composed of 94% N_2, 5% CO_2 and 1% O_2. RIPK1-deficient Jurkat cells were kindly provided by B. Seed. THP-1 cells were kindly provided by J. Kagan (Harvard Medical School). *Ripk1*$^{D138N/D138N}$ MEFs were homemade from the *Ripk1*$^{D138N/D138N}$ mice, which were kindly provided by M. Kelliher (University of Massachusetts) and M. Pasparakis (University of Cologne). *Ripk3* knockout MEFs were homemade from the *Ripk3* knockout mice, which were kindly provided by V. Dixit of Genentech. *Mlkl* knockout MEFs were kindly provided by X. Wang (National Institute of Biological Sciences, Beijing, China). *Tnfr1/2* double knockout MEFs were homemade from *Tnfr*1/2 knockout mice (The Jackson Laboratory). *Egln1*$^{-/-}$, *Egln2*$^{-/-}$, *Egln3*$^{-/-}$ and *Vhl*$^{fl/fl}$

MEFs were kindly provided by W. G. Kaelin Jr. *cIAP1/2* double knockout MEFs were kindly provided by J. Silke (The Walter and Eliza Hall Institute of Medical Research).

The following chemicals in cell cultures were used: DFO (D9533; Sigma–Aldrich), $CoCl_2$ (409332; Sigma–Aldrich), FG-4592 (S1007; Selleckchem), ketoglutarate (A610290; Sangon Biotech), ascorbate (A500830; Sangon Biotech), $FeSO_4$ (A110387; Sangon Biotech) and catalase (NC9204367; Worthington Biochemical).

Generation and immortalization of MEFs

MEFs were isolated from E11–13 embryos using trypsin/EDTA and sieved through a 70-μm filter. Primary MEFs were cultured in high-glucose Dulbecco's modified Eagle medium supplemented with 15% FBS, non-essential amino acids, sodium pyruvate, penicillin, streptomycin and amphotericin B. At passages 4–6, primary MEFs were immortalized by transfection with the simian virus 40 large T antigen-expressing plasmid (22298; Addgene) using Lipofectamine 2000.

Plasmid construction

Constructs of pcDNA3-HA-pVHL, pBabe-HA-pVHL, pCMV-Flag-EglN1, pCMV-Flag-EglN2 and pCMV-Flag-EglN3 were described previously[36,52]. pCMV-GST-pVHL, pCMV-GST-EglN1, pCMV-GST-EglN1-N (amino acids 1–180) and pCMV-GST-EglN1-C (amino acids 181–425) were cloned into mammalian expression GST fusion vectors. Full-length complementary DNAs for mouse and human RIPK1 were PCR amplified from the plasmid library and cloned into pcDNA3.1 using Phanta Max Super-Fidelity DNA Polymerase (Vazyme Biotech) with the appropriate tags. Mutant human RIPK-P195A was generated using the Mut Express II mutagenesis kit (Vazyme Biotech). To generate CRISPR-mediated knockout cell lines, sgRNAs were sub-cloned into the pLenti-CRISPRv2 GFP vector (Addgene). The sgRNA sequences for human VHL were CATACGGGCAGCACGACGCG (sg1) and GCGATTGCAGAAGATGACCT (sg2). All plasmids were verified by DNA sequencing and the details of the plasmid sequences are available upon request.

Antibodies

The following antibodies were used: RIPK1 (610459 (BD Biosciences) and 3493 (Cell Signaling Technology)), p-RIPK1-S166 (65746 and 31122; Cell Signaling Technology), p-RIPK3 (91702 and 57220; Cell Signaling Technology), RIPK3 (13526 and 95702; Cell Signaling Technology), MLKL (ab172868; Abcam), p-MLKL (ab187091 (Abcam) and 37333 (Cell Signaling Technology)), cIAP1 (ALX-803–335-C100; Enzo Life Sciences), HNF4α (ab41898; Abcam), CD45 (AF114-SP; R&D Systems), VE-Cadherin (CAF1002; R&D Systems), α-SMA (ab7817; Abcam), CD68 (97778; Cell Signaling Technology), VHL (68547; Cell Signaling Technology), EglN1 (4835; Cell Signaling Technology), HIF-1β (5537; Cell Signaling Technology), HIF-1α (36169; Cell Signaling Technolog), HIF-2α (NB100–122; Novus Biologicals), EglN2 (NB100–310SS; Novus Biologicals), EglN3 (NB100–139SS; Novus Biologicals), anti-Hydroxyproline (ab37067; Abcam), TNFR1 (13377; Cell Signaling Technology), CC3 (9664; Cell Signaling Technology), BNIP3 (3769; Cell Signaling Technology), BNIP3L (12396; Cell Signaling Technology), S100A8 (PA5–95847; Invitrogen), CD11b (101202; BioLegend); Ly-6G (127602; BioLegend),

Flag M2 (F1804; Sigma–Aldrich), HA (sc-805; Santa Cruz Biotechnology), GST (2625; Cell Signaling Technology), Tubulin (PM054; MBL), β-actin (sc81178; Santa Cruz Biotechnology), anti-Flag agarose beads (A2220; Sigma–Aldrich), anti-HA agarose beads (A2095; Sigma–Aldrich), peroxidase-conjugated anti-mouse secondary antibody (A4416; Sigma–Aldrich) and peroxidase-conjugated anti-rabbit secondary antibody (A4914; Sigma–Aldrich).

The rabbit-derived polyclonal RIPK1-P195-OH antibodies were generated by ABclonal. The antigen sequence used for immunization was RIPK1 (amino acid residues 194–201)–A(Hyp)EHLNDV–C, where Hyp represents hydroxyl-proline residue Pro195 in the synthetic peptide. The antibodies were affinity purified using an antigen peptide column, but they were not counter selected on unmodified antigens.

Immunoblots and immunoprecipitation

Cells were lysed in EBC buffer (50 mM Tris (pH 7.5), 120 mM NaCl and 0.5% NP-40) supplemented with protease inhibitors (cOmplete Mini; Roche) and phosphatase inhibitors (Phosphatase Inhibitor Cocktail Sets I and II; Calbiochem). The lysates were then resolved by sodium dodecyl sulfate polyacrylamide gel electrophoresis (SDS-PAGE) and immunoblotted with the indicated antibodies. For immunoprecipitation, 1 mg lysates were incubated with the appropriate sepharose beads for 4 h at 4 °C. Immunocomplexes were washed three times with buffer (20 mM Tris (pH 8.0), 100 mM NaCl, 1 mM EDTA and 0.5% NP-40) before being resolved by SDS-PAGE and immunoblotted with the indicated antibodies. For endogenous co-immunoprecipitation assay, cells were lysed with NP-40 buffer (10 mM Tris-HCl (pH 7.5), 150 mM NaCl, 0.5% NP-40, protease inhibitor cocktail, 5% glycerol, 10 mM NaF and 1 mM phenylmethylsulfonyl fluoride). Whole-cell lysates obtained by centrifugation were incubated with 5 mg antibody and protein G agarose beads (Invitrogen) overnight at 4 °C. The immunocomplexes were then washed with NP-40 buffer three times and separated by SDS-PAGE for further western blotting assays.

Isolation of NP-40-soluble and NP-40-insoluble/urea-soluble fractions

Cells were lysed in EBC buffer (as above) supplemented with protease inhibitors (cOmplete Mini; Roche) and phosphatase inhibitors (Phosphatase Inhibitor Cocktail Sets I and II; Calbiochem). Lysates were flash frozen on dry ice followed by centrifugation at 10,000*g* for 10 min. The resultant supernatants were collected (NP-40-soluble fractions) and boiled in 1× SDS-PAGE buffer. Pellets (NP-40 insoluble) were lysed in EBC buffer with 6 M urea overnight at 4 °C and then boiled in 1× SDS-PAGE buffer.

Analysis of cytotoxicity and viability

Cell death was analysed by measuring plasma membrane integrity to incorporate propidium iodide. Total cell numbers and propidium iodide-positive cells were counted under an inverted fluorescence microscope. The rates of cell death were also measured in triplicate or quadruplicate in a 96- or 384-well plate using SYTOX Green Nucleic Acid Stain (Invitrogen) or a ToxiLight Non-destructive Cytotoxicity BioAssay Kit (Lonza). The intensity of luminescence was determined in an EnSpire Multimode Plate Reader (PerkinElmer). The rates of cell viability were determined by ATP-Glo Luminescent Cell

Viability Assay (Promega) following the manufacturer's protocol. The results are expressed as percentages of luminescence intensity per well after deducting the background signal in a blank well and are compared with the viability in non-treated wells.

Histology and immunochemistry

Animals were sacrificed and perfused with phosphate-buffered saline followed by 4% paraformaldehyde. Then, 20 μm sections were prepared on a cryostat. For immunostaining, tissue sections were mounted and blocked with 10% normal goat serum and 1% bovine serum albumin, then incubated with primary antibodies at 4 °C overnight. Images were collected with a Nikon Ti-E confocal microscope equipped with an A1R scan head with a spectral detector and resonant scanners and acquired with Nikon NIS-Elements software.

TUNEL assay

TUNEL assay was used to detect dead cells with DNA fragmentation using an In Situ Cell Death Detection Kit, POD (Roche), following the manufacturer's protocol.

ALT, AST and bilirubin measurement

To determine the liver injury at the enzymatic level, the serum ALT activity was measured with an EnzyChrom Alanine Transaminase Assay Kit (EALT-100; BioAssay Systems) and a kinetic method (A525–240; Teco Diagnostics) according to the manufacturers' instructions. Serum AST activity was measured with an EnzyChrom Aspartate Transaminase Assay Kit (EASTR-100; BioAssay Systems) or a kinetic method (A560-24; Teco Diagnostics) according to the manufacturers' instructions. Serum bilirubin was measured with a Bilirubin Assay Kit (MAK126; Sigma–Aldrich) according to the manufacturer's instructions.

Serum collection and cytokine analysis

All cytokines and chemokines were measured in serum from the mice after anaesthesia. The blood samples were centrifuged at 1,500*g* for 10 min at 4 °C and the supernatants were aspirated and separated into 500 μl aliquots. The concentrations of serum cytokines and chemokines were analysed by multiplexed enzyme-linked immunosorbent assay or by a customized Luminex immunoassay following the manufacturer's instructions (LXSAMSM-08; R&D Systems). Assays were read using a Multiskan GO Microplate Spectrophotometer (Thermo Fisher Scientific) and a Luminex 200 multiplexing instrument (Merck Millipore).

RNA isolation and real-time reverse transcription PCR analyses

Total RNA from cells was extracted using an RNeasy kit (Qiagen) according to the manufacturer's instructions. Complementary DNA was then diluted and used for real-time PCR with gene-specific primers using SYBR Select Master Mix (Thermo Fisher Scientific). The primers used for the PCR reactions are listed in Supplementary Table 2.

Protein expression and purification

Human VHL (amino acids 55–213), elongin C (amino acids 17–122) and elongin B (amino acids 1–118) proteins were co-expressed in *Escherichia coli* BL21(DE3) as GST or

Trx-6×His fusion proteins in modified pGEX-4T-1 (GE Healthcare), pRSF-Deut1 (Novagen) and pAcyc-Deut1 vectors (Novagen), respectively. EGLN1 (amino acids 1–426) was expressed as a Trx-6×His fusion protein in *E. coli*. Cells were harvested by centrifugation, disrupted using a high-pressure homogenizer (FB-110S; Shanghai Litu) and purified with Ni^{2+} affinity resin (GE Healthcare). Proteins were further purified by size exclusion chromatography on a Superdex 200 pg 26/60 column (GE Healthcare) in a buffer containing 20 mM Tris-HCl (pH 7.5), 100 mM NaCl and 5 mM β-mercaptoethanol.

Peptide synthesis

Amino-terminal biotinylated peptides used for pull-down assays were synthesized at LifeTein. The peptides for in vitro hydroxylation and fluorescence polarization assay were synthesized by the commercial vendor ChinaPeptides. The sequences were as follows: Bio-KNGGTLYYMAPEHLNDVNAKP (hRIPK1-WT(195)), Bio-KNGGTLYYMAP(OH)EHLNDVNAKP (hRIPK1-P195-OH), Bio-EAN PEARPTFPGIEEKFRPFY (hRIPK1-WT(279)), Bio-EANPEARPTFP(OH) GIEEKFRPFY (hRIPK1-P279-OH), DLDLEMLAPYIPMDDDFQLR (HIF-1α-WT (aa556–575)) and DLDLEMLAP(OH)YIPMDDDFQLR (HIF-1α-OH).

The peptides for in vitro hydroxylation, fluorescence polarization assay and crystallization were synthesized by the commercial vendor ChinaPeptides. The sequence was as follows: T_{189}LYYMA(OH)EHLN DVNA$_{203}$ (hRIPK1-WT(195))

Peptides were diluted into 1 mM for further biochemical assays.

Peptide pull-down assay

Biotin-labelled RIPK1 peptides with or without hydroxylation at Pro195 or Pro279 were immobilized on streptavidin beads (Agilent Technologies). After washing out the excessive unbound peptides, VCB complex was added and incubated with the loaded beads for 30 min at 4 °C. After washing five times with a buffer containing 50 mM Tris-HCl (pH 7.5), 150 mM NaCl and 0.5% (vol/vol) NP-40, the beads were boiled in SDS-PAGE sample buffer and analysed by SDS-PAGE.

Fluorescence polarization assay

Synthetic RIPK1 peptide (T_{189}LYYMA(Hyp)EHLNDVNA$_{203}$) was labelled with fluorescein isothiocyanate according to the protocol of the chemical supplier (Thermo Fisher Scientific). The fluorescence polarization was measured with a microplate reader (Tecan GENios Pro; Tecan).

In vitro hydroxylation reaction

The assay system was set up according to previous reports[52,53] using *E. coli*-expressed EGLN1 enzyme (amino acid residues 1–426) and synthetic peptide (KNGGTLYYMAPEHLNDVNAKP) or RIPK1 kinase domain (1–312) purified from insect cells. The reaction mixture was incubated at 37 °C for 1 h containing 50 mM Tris-HCl (pH 7.5), 4 mM ascorbate, 300 μM ketoglutarate, 100 μM $FeSO_4$, 0.7 mg ml^{-1} catalase, 50 μM

EGLN1 and 100 μM substrate (peptide or RIPK1 kinase domain). The reaction solution was sent directly for mass spectrometry analysis.

Mass spectrometry analysis

For mass spectrometry analysis, anti-Flag immunoprecipitations were performed with the whole-cell lysates derived from three 10 cm dishes of HEK293 cells. The immunoprecipitation proteins were resolved by SDS-PAGE and identified by Coomassie staining. The band containing RIPK1 was reduced with 10 mM dithiothreitol for 30 min, alkylated with 55 mM iodoacetamide for 45 min and in-gel digested with trypsin enzymes. The resulting peptides were extracted from the gel and analysed by microcapillary reversed-phase (C18) liquid chromatography with tandem mass spectrometry using a high-resolution Orbitrap Elite (Thermo Fisher Scientific) in positive ion data-dependent acquisition mode (Top 6) via higher-energy collisional dissociation coupled to a Proxeon EASY-nLc II nano-HPLC system[52]. Tandem mass spectrometry data were searched against the UniProt human protein database (version 2021_0616 containing 20,600 entries) using Mascot 2.7 (Matrix Science) and data analysis was performed using Scaffold Q+S 5.0 software (Proteome Software). Peptides and modified peptides were accepted if they passed a 1% false discovery rate threshold.

Crystallization and structure determination

For crystallization, the VCB protein complex (VHL amino acids 55–213, elongin C amino acids 17–122 and elongin B amino acids 1–118) was mixed with a fivefold molar ratio of synthetic RIPK1 peptide (T_{189}LYYMA(Hyp) EHLNDVNA_{203}), resulting in a final protein concentration of 10 mg ml^{-1}. The mixture was used to set up sitting-drop vapour diffusion crystallization with a reservoir buffer containing 100 mM sodium cacodylate (pH 6.5), 100 mM magnesium acetate and 15% (wt/vol) PEG 6000. After ~10 d, crystals were harvested in the reservoir buffer with additional 20% (vol/vol) glycerol and flash frozen in liquid nitrogen. Diffraction datasets were collected at the beam line BL17U1 of the Shanghai Synchrotron Radiation Facility. The phase was obtained by molecular replacement, with the VCB structure (Protein Data Bank (PDB) ID: 4AJY) as a searching template, using the software suite Phenix. Further structure refinement was performed in Coot and Phenix.

Statistics and reproducibility

The data for cell death measurement are presented as means ± s.d. of one representative experiment. Each experiment was repeated at least three times. Mouse data are presented as means ± s.e.m. of the indicated *n* values. Quantification of immunoblots was performed by densitometry analysis using ImageJ 1.52a software with the same parameters. The data of three independent experiments were quantified by ImageJ. The bars represent means ± s.e.m. of $n = 3$ independent experiments. Three independent experiments were performed in parallel and the gels or blots were processed in parallel. Statistical parameters, including exact sample sizes (*n*), post-hoc tests and statistical significance, are reported in the figure captions. Statistical analyses were performed with Microsoft Excel for Mac (version 15.36) and GraphPad Prism 8.0. The normality of the samples was checked using the Shapiro–Wilk test before statistical analysis. For a normal distribution, either an unpaired two-tailed Student's *t*-test (for comparison between two groups) or one-way analysis of variance

(ANOVA) with post-hoc Dunnett's test (for comparisons among multiple groups with a single control) was applied. For non-normal distributions, non-parametric statistical analysis was performed by Mann–Whitney *U*-test (for two groups) or Kruskal–Wallis test followed by Dunnett's test (for multiple comparisons). Statistical comparisons for a series of data collected at different time points were conducted by two-way ANOVA. The significance of in vivo survival data was determined by log-rank (Mantel–Cox) test. When $P < 0.05$, the data were considered statistically significant. No statistical method was used to pre-determine sample size, but our sample sizes are similar to those reported in previous publications. For all experiments, samples were randomly allocated to groups. For the in vivo experiments, the blinding was performed when the in vivo data were collected and analysed between experimental and control groups. For experiments other than the in vivo studies, the investigators were blinded during data collection and analysis where possible. However, for the cell death assay in vitro study blinding was not necessary as the results of cell viability were determined by an automated pipeline using a fluorescence plate reader in an unbiased manner. No animals or data points were excluded from the analysis.

Extended Data

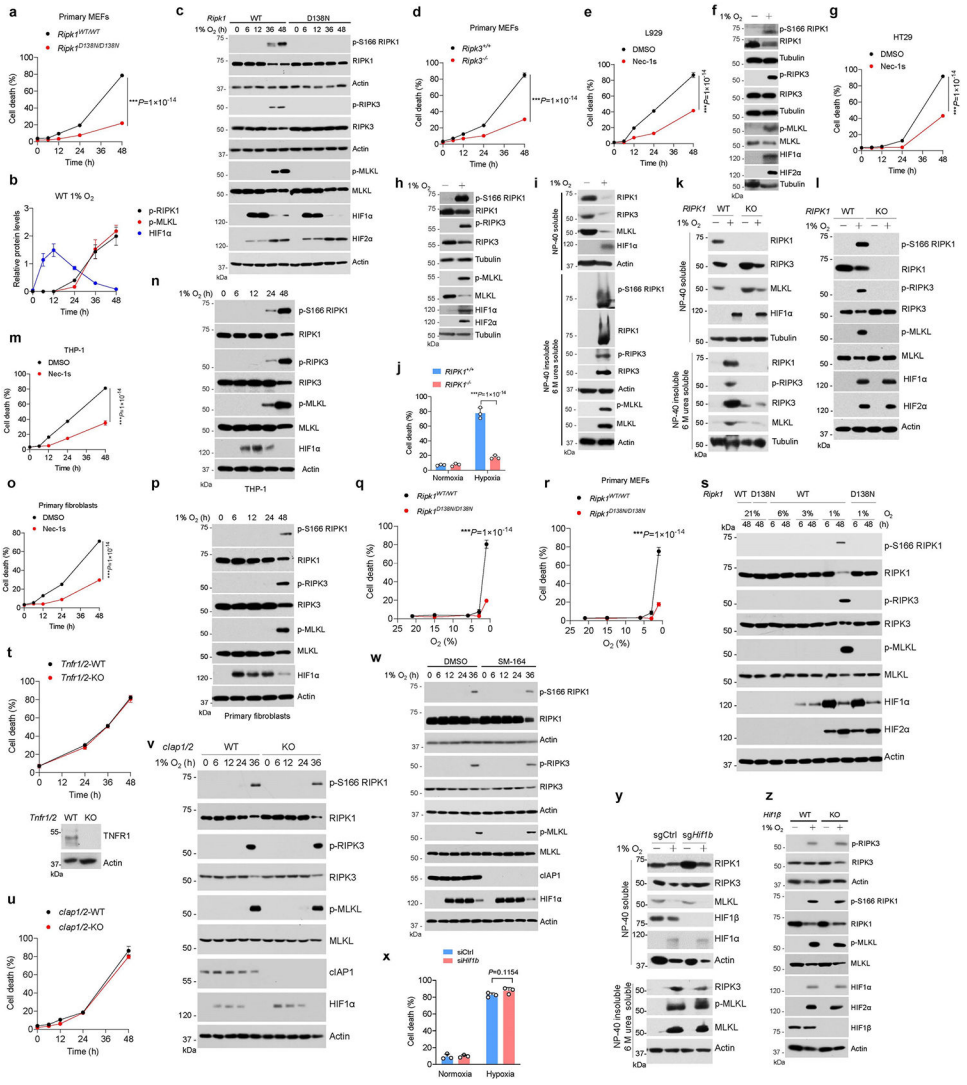

Extended Data Fig. 1 |. Hypoxia induces RIPK1 activity.

(**a-d**) Primary MEFs of indicated genotypes were exposed to 1% O_2 for different times. Cell death was measured by PI uptake assay. Data are mean ± s.d. of $n = 3$ biological independent samples. Two-way ANOVA (a, d). Quantified values for western blot images for Fig. 1b. Data are presented as mean ± s.e.m. of n = 3 independent experiments (b). (**e-g**) L929 (e, f) and HT-29 (g) cells were exposed to 1% O_2 in the presence or absence of Nec-1s. Cell death was measured by PI uptake assay. Data are mean ± s.d. of $n = 3$ biological independent samples. Two-way ANOVA. Nec-1s, 25 μM (e, g). (**h-p**) HT-29 (h, i), Jurkat (j, k, l), THP-1 (m, n), primary fibroblasts (o, p) were exposed to 1% O_2 for 48 h. Cell death was measured by PI uptake assay. Data are mean ± s.d. of n = 3 biological independent samples. Unpaired two-tailed t-test (j, m, o). (**q-s**) Immortalized (q) and primary (r, s) WT or *Ripk1*^{D138N} MEFs were exposed to different oxygen concentrations for 48 h. Cell death was measured by PI uptake assay. Data are mean ± s.d. of n = 3 biological independent samples. Two-way ANOVA (q, r). (**t-z**) MEFs of indicated genotypes (t, u, v, x, y, z) and primary

MEFs treated with or without SM164 (50 nM) (w) were exposed to 1% O_2 for the indicated times. Cell death was measured by PI uptake assay. Data are mean ± s.d. of n = 3 biological independent samples, unpaired two-tailed t-test (t, u, x). Cell lysates were immunoblotted with the indicated antibodies(c,f,h, i, k, l, n, p,s,v, w, y, z). Results are representative of three independent experiments (c,f,h, i, k, l, n, p,s,v, w, y, z).

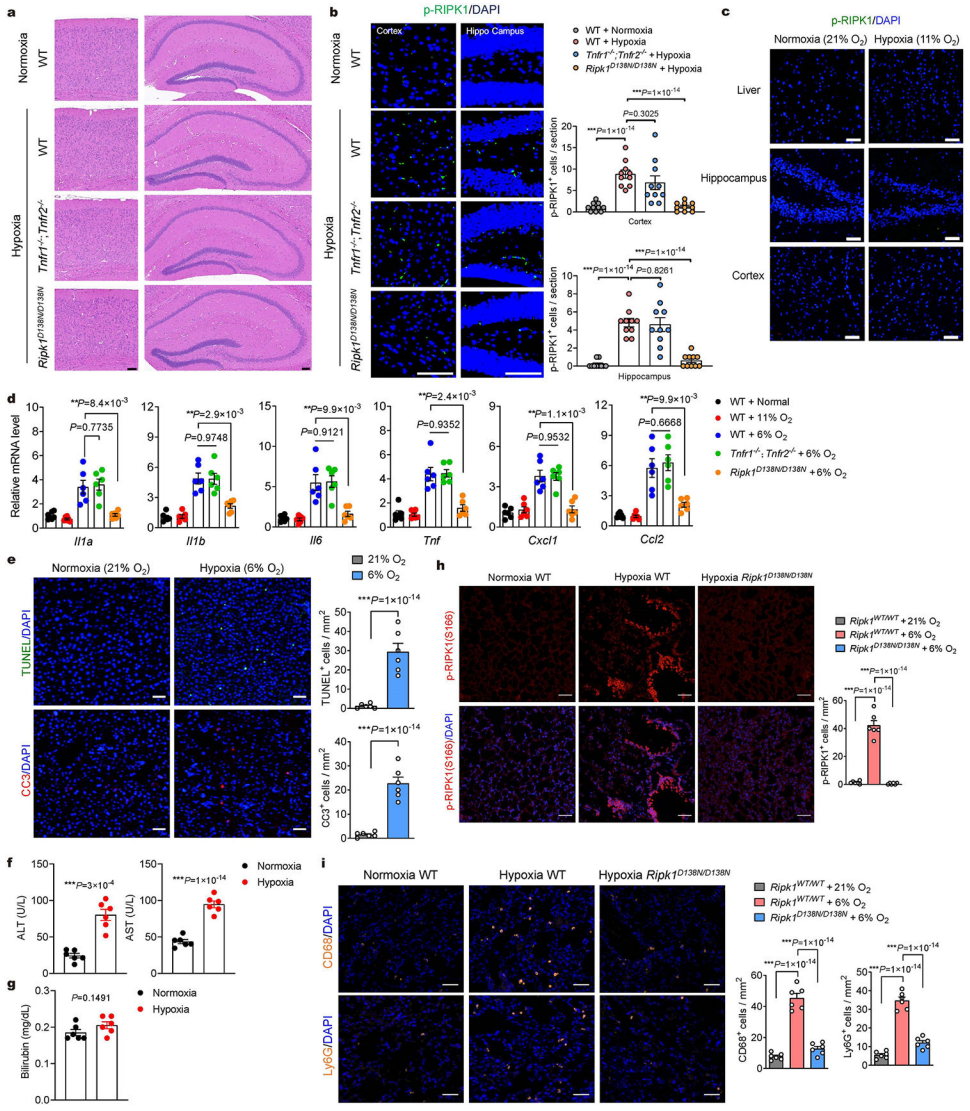

Extended Data Fig. 2 |. Hypoxia promotes RIPK1 activity in vivo.

(**a-i**) **Mice of indicated genotypes** were challenged to hypoxia for 72 h. Histological analysis on brain sections (n = 10) (a), immunostaining for p-RIPK1(S166) on brain sections (n = 10) (b), brain and liver sections (n = 10) (c), qRT-PCR analysis of the mRNA expression of the indicated cytokines and chemokines from brains (n = 6). Data are mean ± s.e.m. One-way ANOVA, post hoc Dunnett's test (d), TUNEL assays and immunostaining for Cleaved caspase-3 (CC3) on liver sections (n = 6). Scale bars, 100 μm. DAPI for nuclei. Microscopic quantification of TUNEL and CC3 positive cells (right). Data are mean ± s.e.m. Unpaired two-tailed t-test (e), serum ALT and AST levels (f), Bilirubin levels (g)

were measured from wild type mice (n = 6). Data are mean ± s.e.m. Unpaired two-tailed t-test, immunostaining for p-RIPK1(S166) (h), CD68 and Ly6G (i) on lung sections (n = 6). Scale bars, 100 μm. DAPI for nuclei. Microscopic quantification of p-S166, CD68 and Ly6G positive cells (right). Data are mean ± s.e.m. One-way ANOVA, post hoc Dunnett's test.

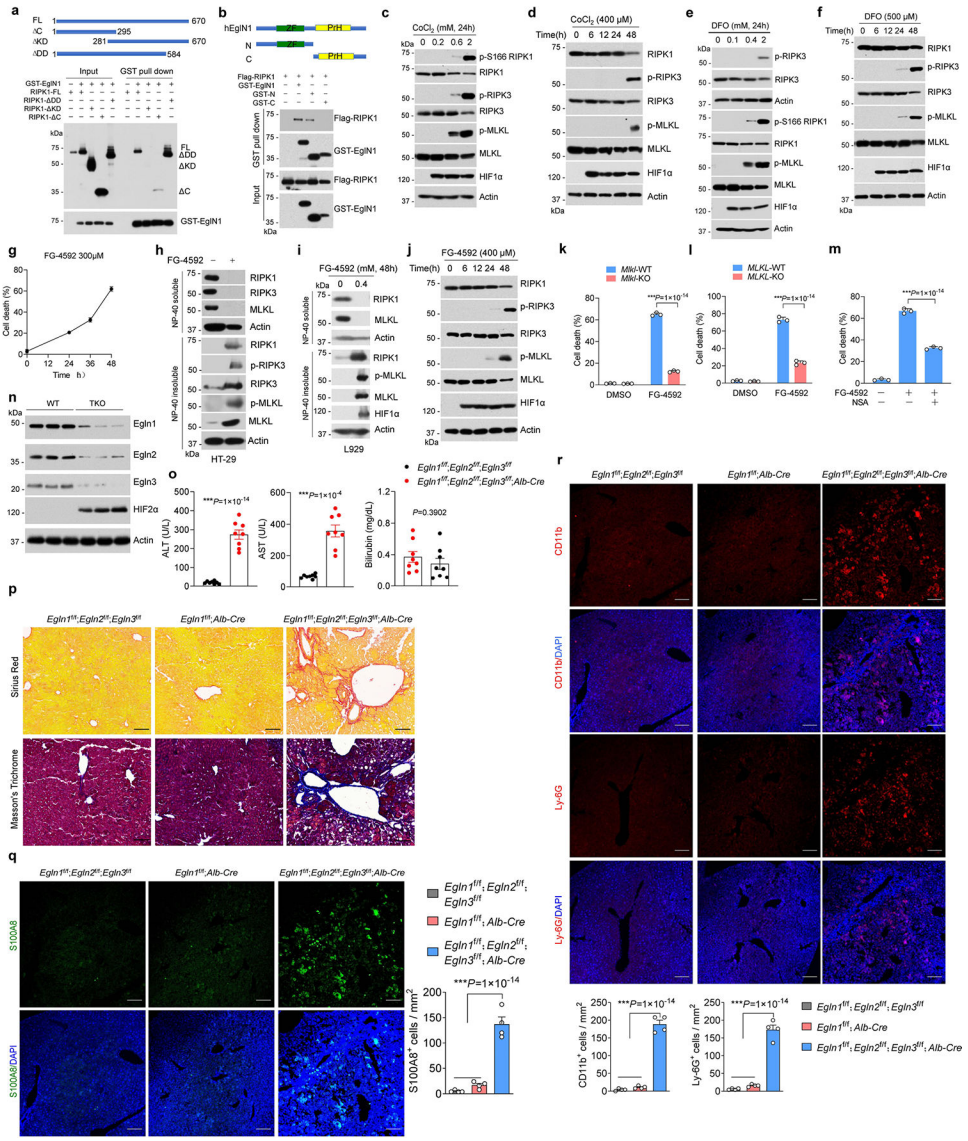

Extended Data Fig. 3 |. Inhibition of EGLN1 promotes RIPK1 activation.

(**a-b**) 293 T cells were transfected with the indicated expression vectors. The lysates were immunoprecipitated with anti-GST, and the immunocomplexes were analysed by immunoblotting using anti-HA (a) or anti-Flag (b). Results are representative of three independent experiments. (**c-m**) MEFs (c, d, e, f, g, j, k), HT-29 cells (h, l, m), L929 cells (i) were treated with $CoCl_2$ (c-d), DFO (e-f), FG-4592 (g, h, j, k, l, m), 10 μM necrosulfonamide (NSA) for 48 h (m) with indicated concentrations or times as indicated. The levels of indicated proteins were determined by immunoblotting, Results are representative of three independent experiments (c, d, e, f, h, i, j). Cell death was measured

by PI uptake assay. Data are mean ± s.d. of $n = 3$ biological independent samples. Unpaired two-tailed t-test (g, k, l, m). (**n-r**) The livers from indicated genotypes at the age of 6 weeks. The levels of Egln were determined by immunoblotting (n = 3), Serum ALT, AST and Bilirubin levels (n = 8), Unpaired two-tailed t-test (o), Masson's trichrome or Sirius Red staining on liver sections (p) (n = 4), immunostaining for proinflammatory cytokine S100A8 (q), CD11b and Ly-6) (r) on liver sections (n = 4). Microscopic quantification of S100A8, CD11b and Ly-6G positive cells (right). Data are means ± s.e.m. One-way ANOVA, post hoc Dunnett's test. DAPI for nuclei. Scale bar, 100 μm.

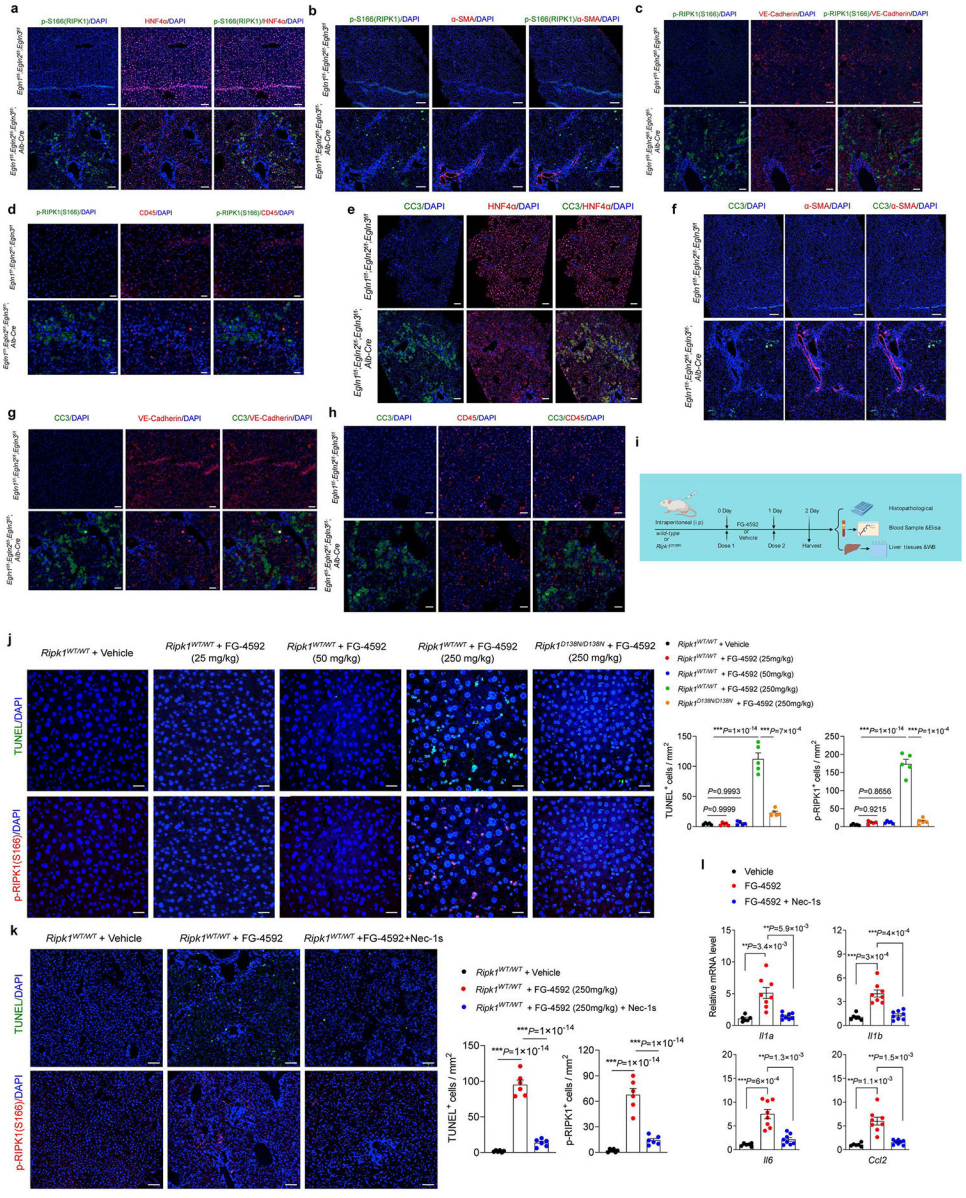

Extended Data Fig. 4 |. Inhibition of Egln activity caused liver damage.
(**a-h**) Co-immunostaining for p-RIPK1(S166) and HNF4α (a), α-SMA (b), VE-Cadherin (c), and CD45 (d), co-immunostaining for CC3 and HNF4α (e), α-SMA (f), VE-Cadherin (g), and CD45 (h) on liver sections from *Egln1*$^{fl/fl}$*::Egln2*$^{fl/fl}$*::Egln3*$^{fl/fl}$ and

Egln1$^{fl/fl}$*::Egln2*$^{fl/fl}$*::Egln3*$^{fl/fl}$*::AlbCre* littermate mice at the age of 6 weeks (n = 4). DAPI for nuclei. Scale bar, 100 μm. (**i**) A schematic representation of FG-4592 induction of RIPK1 activation and inflammation. (**j-l**) Mice of indicated genotypes at the age of 6–8 weeks were intraperitoneally injected with vehicle control or FG-4592 (25 mg/kg, 50 mg/kg or 250 mg/kg body weight) every 24 h for two days (n = 5) (j). WT mice were treated with or without Nec-1s for 7 days, and then were intraperitoneally injected with vehicle control or FG-4592 (250 mg/kg body weight) with or without Nec-1s every 24 h for another two days (n = 6) (k), qRT-PCR analysis of the mRNA expression of the indicated cytokines and chemokines (n = 6 for the Vehicle, n = 8 for FG-4592 or FG-4592+Nec-1s) (l). TUNEL assays and immunostaining for p-RIPK1(S166) on liver sections. DAPI for nuclei. Microscopic quantification of TUNEL and p-RIPK1(S166) positive cells (right). Data are means ± s.e.m. One-way ANOVA, post hoc Dunnett's test. Data are mean ± s.e.m. One-way ANOVA, post hoc Dunnett's test.

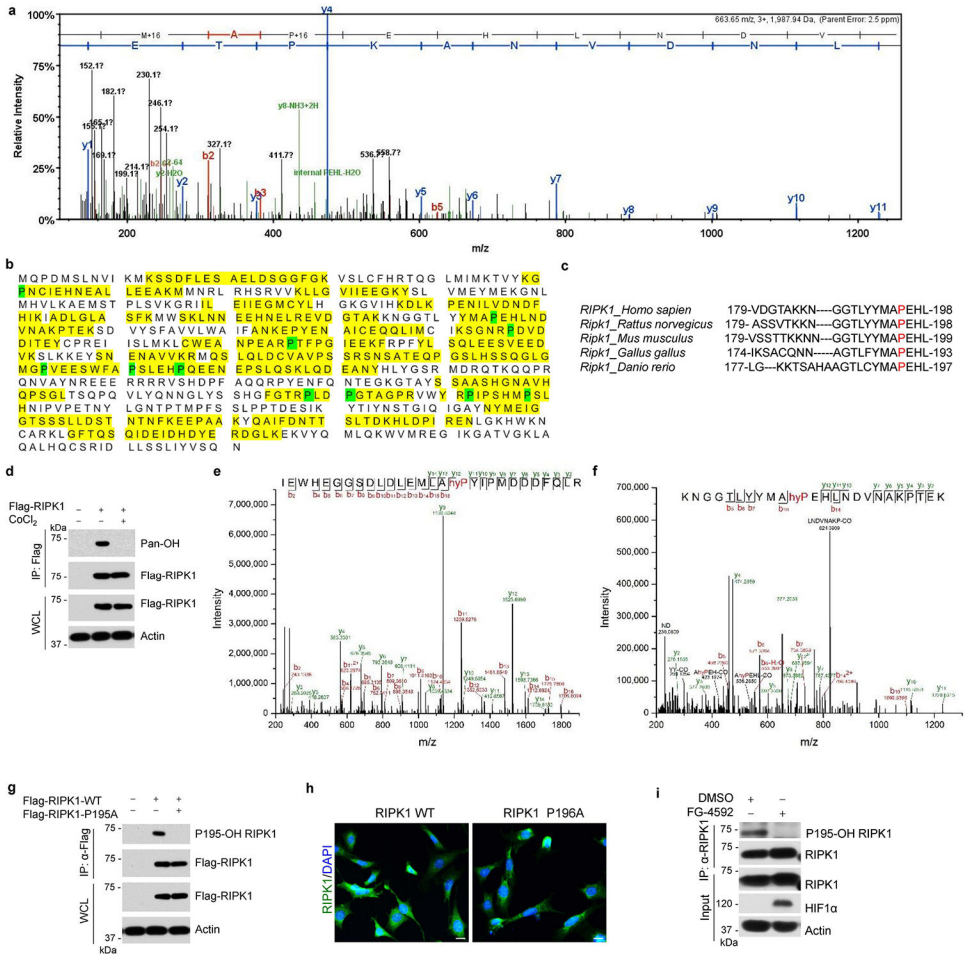

Extended Data Fig. 5 |. EGLN1 hydroxylates RIPK1 to suppress RIPK1 activity.
(**a-b**) 293 T cells were transfected with expression vectors of Flag-RIPK1. Cell lysates were immunoprecipitated with anti-Flag antibody, and the immunocomplexes were analysed by mass spectrometry analysis. MS/MS spectrum to demonstrate the identified hydroxylated RIPK1 peptides at Pro195. The covered amino acids are coloured in yellow, and

hydroxylated Proline amino acids are coloured in green. (**c**) The sequence alignment of human RIPK1 (*Homo sapiens*), rat RIPK1 (*Rattus norvegicus*) and murine RIPK1 (*Mus musculus*) using Clustal Omega is shown around the P195 residue. (**d**) MEFs cells were infected with expression vectors of Flag-mRIPK1 for 24 h, and then treated with the EGLNs inhibitor $CoCl_2$ (400 μM) for another 16 h. The cell lysates were immunoprecipitated with anti-Flag antibody, and the immunocomplexes were analysed by immunoblotting using anti-pan-hydroxylation antibody. Results are representative of three independent experiments. (**e-f**) Mass spectrometry analysis detects the presence of proline hydroxylation event at the RIPK1 Pro195 site in the reaction products of *in vitro* hydroxylation assays with recombinant His-EglN1, and HIF1α peptides were used as positive controls (**e**). Recombinant RIPK1 kinase domain (1–312) purified from insect cells (**f**). (**g**) HT-29 cells were infected with expression vectors of WT or mutant Flag-RIPK1 for 24 h. The cell lysates were immunoprecipitated with anti-Flag antibody, and the immunocomplexes were analysed by western blotting using the anti-p195-OH RIPK1 antibody. Results are representative of three independent experiments. (**h**) Immunostaining for RIPK1 in primary WT or $Ripk1^{P196A}$ MEFs. DAPI for nuclei. Scale bar, 100 μm. Results are representative of three independent experiments. (**i**) 293 T cells were treated with or without FG4592 (50 μM) for 24 h. The cell lysates were immunoprecipitated with anti-RIPK1 antibody, and the immunocomplexes were analysed by immunoblotting using the anti-p195-OH RIPK1 antibody. Results are representative of three independent experiments.

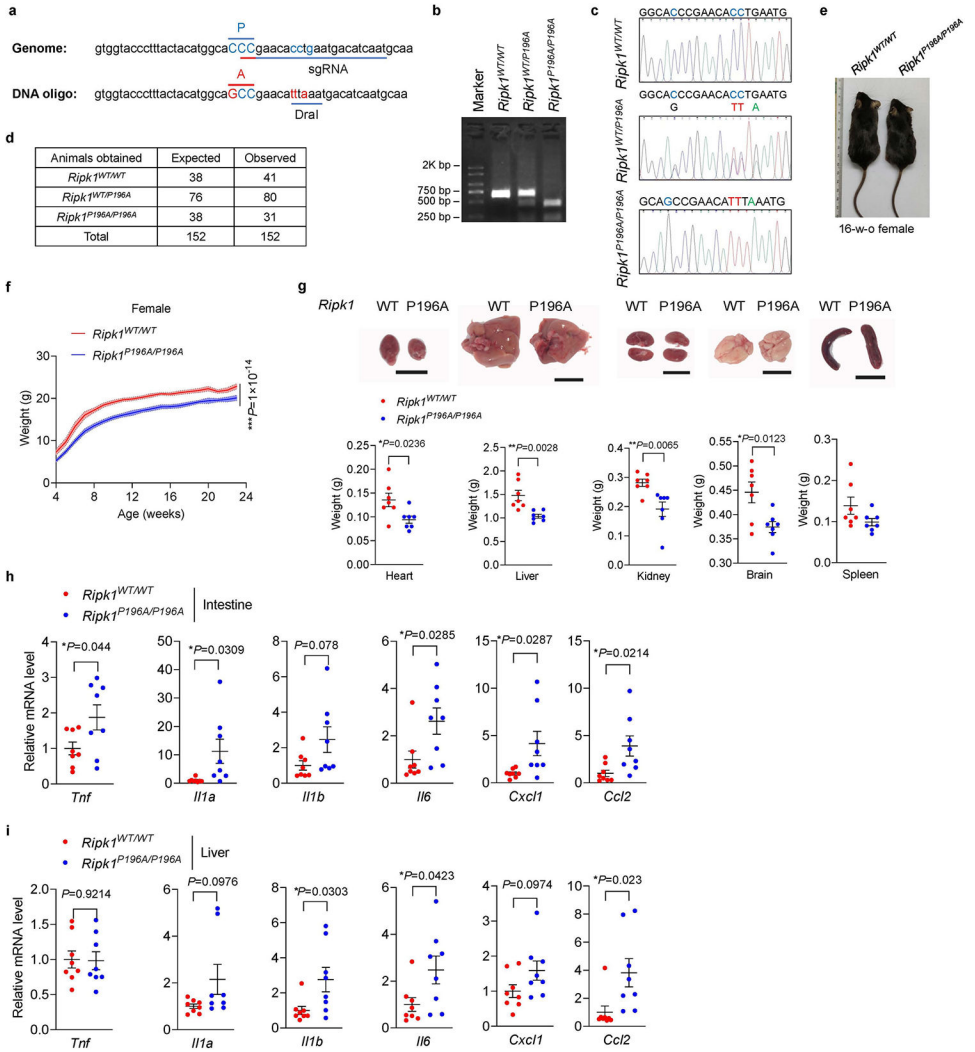

Extended Data Fig. 6 |. RIPK1 P196A mutation promotes cell death and inflammation *in vivo*.

(**a**) schematic diagram of the murine *Ripk1* locus and the *Ripk1*-P196A allele. (**b**-**c**) Tail genotyping for the $Ripk1^{P196A}$ mutant mice. Expected results: $Ripk1^{WT/WT}$ = 730 bp, $Ripk1^{WT/P196A}$ = 730 bp, 500 bp and 230 bp, $Ripk1^{P196A/P196A}$ = 500 bp and 230 bp. Results are representative of four independent experiments (b). (**d**) Numbers of offspring from intercrossing $Ripk1^{P196A/WT}$ parents. (**e**) Representative images of female *WT* and $Ripk1^{P196A/P196A}$ mutant mice at 16 weeks of age. (**f**) Plot of weight changes of the female *WT* and $Ripk1^{P196A/P196A}$ mutant mice at 4–22 weeks of age (*WT*, n = 14, and $Ripk1^{P196A/P196A}$ mutant, n = 16). Data are means ± s.e.m. Two-way ANOVA. (**g**) The indicated tissue weights of $Ripk1^{P196A/P196A}$ mutant mice and the control mice at 16–18 weeks of age (n = 7). Data are means ± s.e.m., Unpaired two-tailed t-test. (**h-i**) qRT-PCR analysis of the mRNA expression of the indicated cytokines and chemokines in RNA isolated from total small intestine (h) and liver (i) from 16–20-week-old mice with the indicated genotypes (n = 8). Data are means ± s.e.m., Unpaired two-tailed t-test.

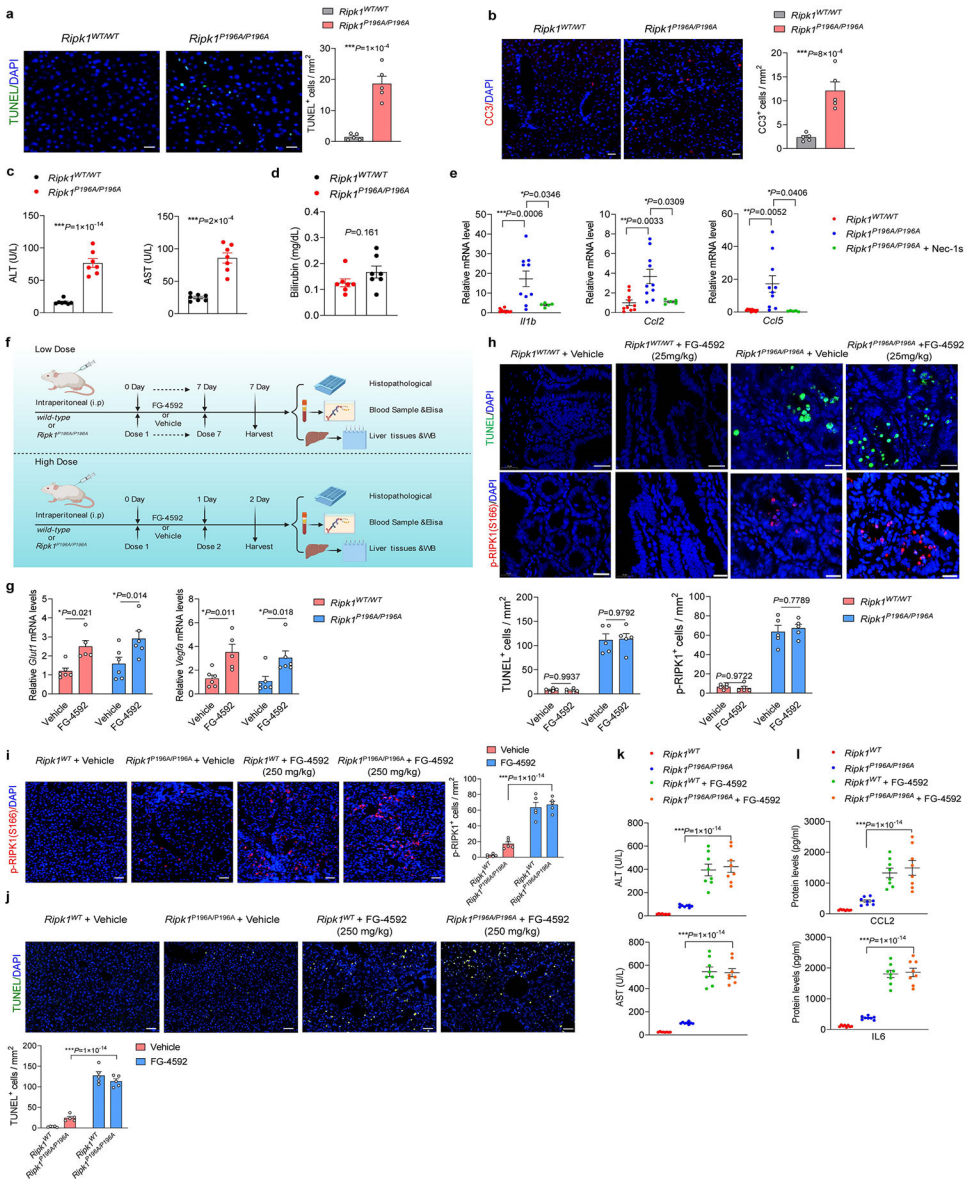

Extended Data Fig. 7 |. Treatment with EGLNs inhibitors promotes RIPK1 activation.

(**a-e**) TUNEL assays (*n* = 5) (a), immunostaining for CC3 (*n* = 5) (b), serum ALT and AST levels (n = 7) (c), serum Bilirubin levels (n = 7) (d) from *Ripk1*$^{P196A/P196A}$ and control mice. DAPI for nuclei. Scale bar, 100 μm. Microscopic quantification of TUNEL, CC3 positive cells (right). Data are means ± s.e.m., Unpaired two-tailed t-test. qRT-PCR analysis of the mRNA expression of the indicated cytokines and chemokines from *Ripk1*$^{P196A/P196A}$ and control mice (n = 10) or *Ripk1*$^{P196A/P196A}$ treated with Nec-1s (n = 5) for 7 days. Data are means ± s.e.m., One-way ANOVA, post hoc Dunnett's test (e). (**f**) A schematic representation of FG-4592 induction of RIPK1 activation and inflammation. (**g-h**) qRT-PCR analysis of the mRNA expression of HIF pathway downstream targets Glut1 and Vegf-a from livers (n = 6) (g), TUNEL assays and immunostaining for p-RIPK1(S166) on intestine sections (n = 5) (h) of 16–20-week-old mice with the indicated genotypes treated with or without FG-4592 at the dose of 25 mg/kg body weight for 7 days. Data are

means ± s.e.m., One-way ANOVA, post hoc Dunnett's test. DAPI for nuclei. Microscopic quantification of TUNEL and p-RIPK1(S166) positive cells (bottom). (**i-l**) Immunostaining for p-RIPK1(S166) (i), TUNEL assays (j), Serum ALT and AST levels (k), ELISA analyses of CCL2 and IL6 protein expression (l) from *Ripk1*$^{P196A/P196A}$ and control mice treated with or without FG-4592 at the dose of 250 mg/kg body weight for 2 days (n = 8). DAPI for nuclei. Scale bar, 100 μm. Microscopic quantification of p-RIPK1(S166) and TUNEL positive cells (right). Data are means ± s.e.m., Unpaired two-tailed t-test.

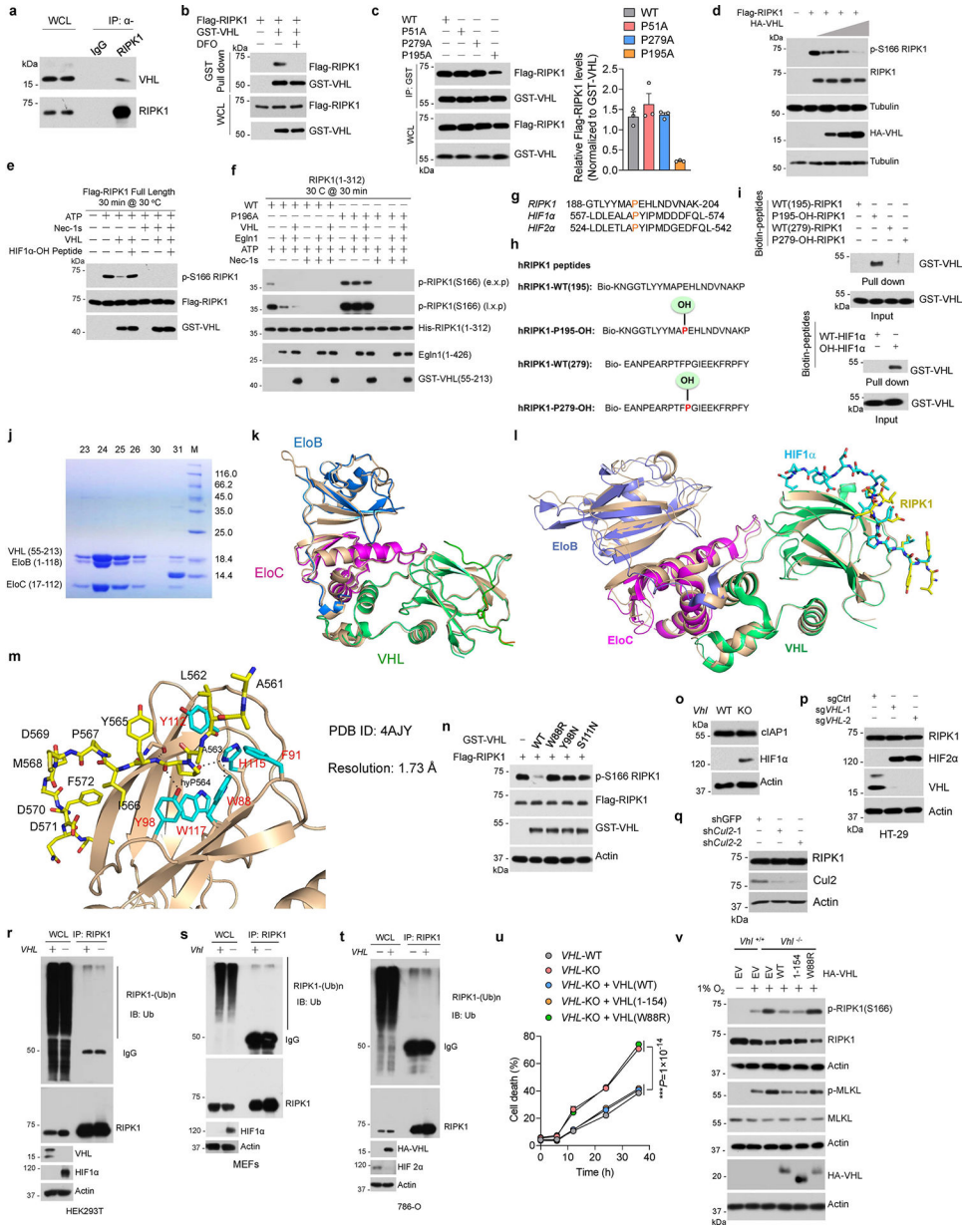

Extended Data Fig. 8 |. pVHL suppresses RIPK1 activity.

(**a-c**) Cell lysates from primary human fibroblasts (a), *RIPK1*$^{-/-}$ HT-29 (b,c) cells infected with indicated expression vectors with (b) or without (c) DFO (200 μM) were immunoprecipitated. The immunocomplexes were immunoblotted. Data are mean ± s.e.m.

of n = 3 independent experiments (c). (**d-f**) Cell lysates from 293 T cells transfected with indicated expression vectors with (e) or without (d) 10 μM Nec-1s, immunoprecipitated using anti-Flag (e), the reaction products of *in vitro* hydroxylation assays (f), incubated with or without 100 μM ATP, 50 μM Nec-1s or purified recombinant VHL and hydroxylated HIF1α peptide at 30 °C for 30 min. The samples were analysed by immunoblotting. (**g**) A sequence alignment of indicated proteins using the Clustal Omega program. (**h**) A schematic representation of various biotinylated synthetic RIPK1-derived peptides. (**i**) Cell lysates from 293 T cells transfected with indicated expression vectors for 24 h, were incubated with RIPK1-derived peptides for 4 h. The immunocomplexes were analysed by immunoblotting. (**j**) Coomassie staining of the bacterially purified recombinant pVHL/Elongin-C/Elongin-B complex. (**k-l**) A structural overlay of pVHL/Elongin-C/Elongin-B bound to either HIF1α or RIPK1. (**m**) Details of interaction between pVHL and HIF-1α (PDB: 4AJY). (**n**) 293 T cells were transfected with indicated expression vectors for 24 h. The levels of indicated proteins were determined by immunoblotting. (**o-q**) Cell lysates from *Vhl* KO MEFs (o), *Vhl* KO HT-29 cells (p), Cul2 knockdown HT-29 cells (q) were immunoblotted. (**r-t**) Cell lysates from *VHL* KO 293 T cells (r), MEFs (s), and 786-O cells (t) were immunoprecipitated with anti-RIPK1 antibody, and immunoblotted. (**u-v**) *Vhl* KO MEFs reconstituted with indicated expression vectors exposed to hypoxia. Cell death was measured by PI uptake assay. Data are mean ± s.d. of $n = 3$ biological independent samples. Two-way ANOVA, post hoc Bonferroni's test (u). Results are representative of three independent experiments. (a-f, i, j,n-t, v).

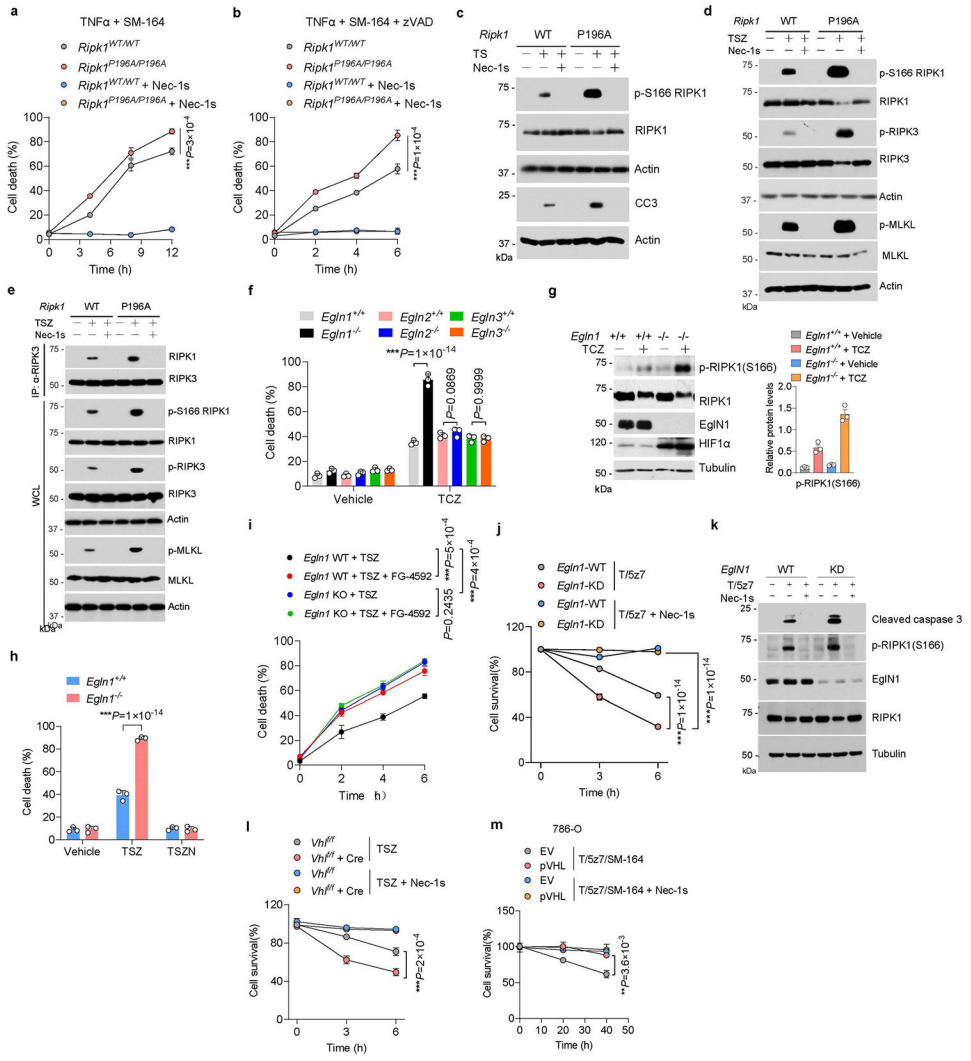

Extended Data Fig. 9 |. Loss of hydroxylation of RIPK1 sensitized cell to cell death.

(**a-e**) Primary WT or *Ripk1*^{P196A} MEFs were treated with TNFα/Smac (a,c), TNFα/Smac/zVAD.fmk (b,d,e) in the presence or absence of Nec-1s. Cell death were measured by PI uptake assay (a,b). The levels of indicated proteins were determined by immunoblotting. Results are representative of three independent experiments (c, d). Cell lysates were immunoprecipitated with anti-RIPK3 antibody, and the immunocomplexes were analysed by western blotting using anti-RIPK1 antibody. Results are representative of three independent experiments (e). Nec-1s, 20 μM; TNF, 10 ng/mL; SM164, 50 nM; zVAD.fmk, 20 μM. Data are mean ± s.d. of n = 3 biological independent samples. Two-way ANOVA. (**f-k**) MEFs of indicated genotypes were treated with TNFα/CHX/zVAD.fmk (f, g), TNFα/Smac/zVAD.fmk (h, i), TNFα/5z7 (j, k) in the presence or absence of Nec-1s (h, j, k) or FG-4592 (i). Cell death were measured by PI uptake assay (f, h, i) and by ATP-Glo assay, Data are mean ± s.d. of n = 3 biological independent samples. Two-way ANOVA, post hoc Bonferroni's test (j). The levels of pS166-RIPK1 and RIPK1 were determined by immunoblotting (g, k). Data are mean ± s.d. of n = 3 biological independent samples. One-way ANOVA, post hoc Dunnett's test (f), Data are mean ± s.e.m. of n = 3 independent

experiments (g, k). Data are mean ± s.d. of n = 3 biological independent samples. Unpaired two-tailed t-test (h), Data are mean ± s.d. of n = 3 biological independent samples. Two-way ANOVA, post hoc Dunnett's test (i). TNFα, 10 ng/mL; zVAD.fmk, 20 μM; CHX, 1 μg/mL; SM164, 50 nM; FG-4592, 200 μM; 5z7, 200 nM; (**l-m**) *Vhl* KO MEFs treated with TNFα/SM-164/zVAD (l) and *VHL*-deficient 786-O cells treated with T/5z7/S (m) in the presence or absence of Nec-1s as indicated for different time followed by cell viability analyses using ATP-Glo assay. Data are means ± s.d. of $n = 3$ biological independent samples. Two-way ANOVA. Compounds used: Nec-1s, 10 μM; TNFα, 10 ng/mL; SM-164, 50 nM; zVAD.fmk, 20 μM; 5z7, 500 nM.

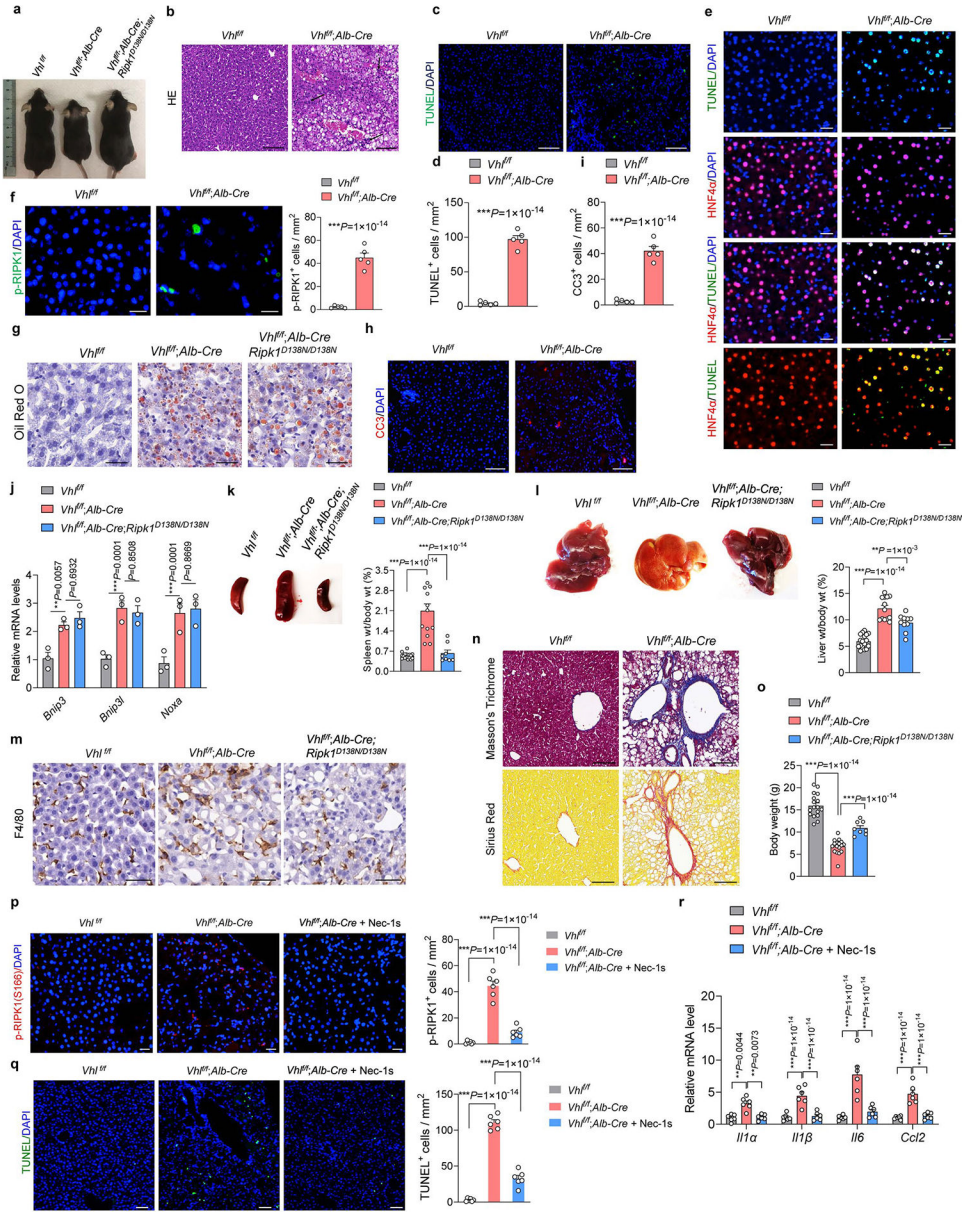

Extended Data Fig. 10 |. *VHL* deletion in liver promotes RIPK1 activation and cell death.

(a) Representative images of mice of indicated genotypes at 5 weeks of age. (b-f) Histological analysis (b), TUNEL assays (c, e), immunostaining for HNF4α(e) and p-RIPK1(S166) (f), microscopic quantification of TUNEL positive cells from (c) and p-RIPK1(S166) (d, f) on liver sections from mice of indicated genotypes (n = 5). DAPI for nuclei. Scale bar, 100 μm. (g-i) Liver sections from mice of indicated genotypes at 5 weeks of age, subjected to Oil Red O staining (n = 3) (g), immunostaining for cleaved caspase-3 (CC3) (n = 5) (h), microscopic quantification of CC3 positive cells from (h) (i). DAPI for nuclei. Scale bar, 100 μm. (j) qRT-PCR analysis of the mRNA expression of the downstream of HIF pathway targets from liver sections of mice of indicated genotypes at the age of 6–8 weeks (n = 3). (k-l) Representative images of spleens (k) and livers (l) of mice of indicated genotypes. Spleen weights (k)(Vhlf/f, n = 17, Vhlf/f;Alb-Cre, n = 13; Vhlf/f;Alb-Cre;Ripk1D138N/D138N, n = 8) and Liver weights (l) (Vhlf/f, n = 17, Vhlf/f;Alb-Cre, n = 13; Vhlf/f;Alb-Cre;Ripk1D138N/D138N, n = 10). (m-n) Representative images of liver sections stained with the F4/80 antibodies (m) and Masson's trichrome or Sirius Red staining (n) from 4-week-old WT, Vhl-LKO or Vhl-LKO;Ripk1D138N/D138N mice (n = 3), Scale bars, 100 μm. (o) Body weight of the control WT (n = 17), Vhl-LKO (n = 17), Vhl-LKO;Ripk1D138N/D138N (n = 8) mice. (p-r) Immunostaining for p-RIPK1(S166) (p), TUNEL assays (q), and qRT-PCR analysis of the mRNA expression of the indicated cytokines and chemokines (r) on liver sections from mice of indicated genotypes treated with Nec-1s for 7 days (n = 6). DAPI for nuclei. Scale bar, 100 μm. Microscopic quantification of p-RIPK1(S166) and TUNEL positive (right). Data are means ± s.e.m., Unpaired two-tailed t-test (d,i). Data are means ± s.e.m., One-way ANOVA, post hoc Dunnett's test(j,k,l,n,o,p,q,r).

Supplementary Material

Refer to Web version on PubMed Central for supplementary material.

Acknowledgements

We thank M. Kelliher (University of Massachusetts) and M. Pasparakis (University of Cologne) for providing the *Ripk1*^{D138N} mice. This work was supported in part by National Institutes of Health grants (R35CA253027 and CA177910 to W.W.). The work of D.X. was supported in part by grants from the National Key R&D Program of China (2022ZD0213200). J.Y. was supported in part by the National Natural Science Foundation of China (82188101, 21837004, 91849204 and 92049303). D.X. and J.Y. were supported in part by the Shanghai Municipal Science and Technology Major Project (2019SHZDZX02), Strategic Priority Research Program of the Chinese Academy of Sciences (XDB39030200 to J.Y. and XDB39030600 to D.X.) and Shanghai Key Laboratory of Aging Studies (19DZ2260400). The work of J.L. was supported by a grant from the National Natural Science Foundation of China (32071297). The work of Y.-R.L. was supported in part by grants from the Career Development Award, Academia Sinica Taiwan (AS-CDA-110-L07 to Y.-R.L) and Ministry of Science and Technology Taiwan (110–2320-B-001–029-MY2 to Y.-R.L). We thank W.W. and J.Y. laboratory members for critical reading of the manuscript, as well as members of the W.W., J.Y. and W.G.K. laboratories for helpful discussions.

Data availability

Coordinates and structure factors have been deposited in the PDB under the accession code 7CJB. The structure of VCB proteins in complex with a peptide (residue 557–574 with Pro564 hydroxylated) of HIF-1α has been deposited in the PDB under the accession code 4AJY. Source data are provided with this paper. All other data supporting the findings of this study are available from the corresponding authors upon reasonable request.

References

1. Eltzschig HK, Bratton DL & Colgan SP Targeting hypoxia signalling for the treatment of ischaemic and inflammatory diseases. Nat. Rev. Drug Discov. 13, 852–869 (2014). [PubMed: 25359381]
2. Eltzschig HK & Eckle T Ischemia and reperfusion—from mechanism to translation. Nat. Med. 17, 1391–1401 (2011). [PubMed: 22064429]
3. Pasparakis M & Vandenabeele P Necroptosis and its role in inflammation. Nature 517, 311–320 (2015). [PubMed: 25592536]
4. Yuan J, Amin P & Ofengeim D Necroptosis and RIPK1-mediated neuroinflammation in CNS diseases. Nat. Rev. Neurosci. 20, 19–33 (2019). [PubMed: 30467385]
5. Xu D et al. TBK1 suppresses RIPK1-driven apoptosis and inflammation during development and in aging. Cell 174, 1477–1491.e19 (2018). [PubMed: 30146158]
6. Sun L et al. Mixed lineage kinase domain-like protein mediates necrosis signaling downstream of RIP3 kinase. Cell 148, 213–227 (2012). [PubMed: 22265413]
7. Wang H et al. Mixed lineage kinase domain-like protein MLKL causes necrotic membrane disruption upon phosphorylation by RIP3. Mol. Cell 54, 133–146 (2014). [PubMed: 24703947]
8. Green DR The coming decade of cell death research: five riddles. Cell 177, 1094–1107 (2019). [PubMed: 31100266]
9. Degterev A et al. Chemical inhibitor of nonapoptotic cell death with therapeutic potential for ischemic brain injury. Nat. Chem. Biol. 1, 112–119 (2005). [PubMed: 16408008]
10. Linkermann A et al. Two independent pathways of regulated necrosis mediate ischemia-reperfusion injury. Proc. Natl Acad. Sci. USA 110, 12024–12029 (2013). [PubMed: 23818611]
11. Adameova A et al. Evidence of necroptosis in hearts subjected to various forms of ischemic insults. Can. J. Physiol. Pharmacol. 95, 1163–1169 (2017). [PubMed: 28472590]
12. Rosenbaum DM et al. Necroptosis, a novel form of caspase-independent cell death, contributes to neuronal damage in a retinal ischemia-reperfusion injury model. J. Neurosci. Res. 88, 1569–1576 (2010). [PubMed: 20025059]
13. Naito MG et al. Sequential activation of necroptosis and apoptosis cooperates to mediate vascular and neural pathology in stroke. Proc. Natl Acad. Sci. USA 117, 4959–4970 (2020). [PubMed: 32071228]
14. Crifo B et al. Hydroxylase inhibition selectively induces cell death in monocytes. J. Immunol. 202, 1521–1530 (2019). [PubMed: 30700584]
15. Polykratis A et al. Cutting edge: RIPK1 kinase inactive mice are viable and protected from TNF-induced necroptosis in vivo. J. Immunol. 193, 1539–1543 (2014). [PubMed: 25015821]
16. Degterev A et al. Identification of RIP1 kinase as a specific cellular target of necrostatins. Nat. Chem. Biol. 4, 313–321 (2008). [PubMed: 18408713]
17. Ofengeim D et al. Activation of necroptosis in multiple sclerosis. Cell Rep. 10, 1836–1849 (2015). [PubMed: 25801023]
18. Zhang DW et al. RIP3, an energy metabolism regulator that switches TNF-induced cell death from apoptosis to necrosis. Science 325, 332–336 (2009). [PubMed: 19498109]
19. Cho YS et al. Phosphorylation-driven assembly of the RIP1–RIP3 complex regulates programmed necrosis and virus-induced inflammation. Cell 137, 1112–1123 (2009). [PubMed: 19524513]
20. He S et al. Receptor interacting protein kinase-3 determines cellular necrotic response to TNF-α. Cell 137, 1100–1111 (2009). [PubMed: 19524512]
21. Bertrand MJ et al. cIAP1 and cIAP2 facilitate cancer cell survival by functioning as E3 ligases that promote RIP1 ubiquitination. Mol. Cell 30, 689–700 (2008). [PubMed: 18570872]
22. Stroka DM et al. HIF-1 is expressed in normoxic tissue and displays an organ-specific regulation under systemic hypoxia. FASEB J. 15, 2445–2453 (2001). [PubMed: 11689469]
23. Jain IH et al. Hypoxia as a therapy for mitochondrial disease. Science 352, 54–61 (2016). [PubMed: 26917594]
24. Vergadi E et al. Early macrophage recruitment and alternative activation are critical for the later development of hypoxia-induced pulmonary hypertension. Circulation 123, 1986–1995 (2011). [PubMed: 21518986]

25. Florentin J et al. Inflammatory macrophage expansion in pulmonary hypertension depends upon mobilization of blood-borne monocytes. J. Immunol. 200, 3612–3625 (2018). [PubMed: 29632145]
26. Yu YA et al. Nonclassical monocytes sense hypoxia, regulate pulmonary vascular remodeling, and promote pulmonary hypertension. J. Immunol. 204, 1474–1485 (2020). [PubMed: 31996456]
27. Lee P, Chandel NS & Simon MC Cellular adaptation to hypoxia through hypoxia inducible factors and beyond. Nat. Rev. Mol. Cell Biol. 21, 268–283 (2020). [PubMed: 32144406]
28. Wu K et al. Stabilization of HIF-1α by FG-4592 promotes functional recovery and neural protection in experimental spinal cord injury. Brain Res. 1632, 19–26 (2016). [PubMed: 26707978]
29. Shivaraju M et al. Airway stem cells sense hypoxia and differentiate into protective solitary neuroendocrine cells. Science 371, 52–57 (2021). [PubMed: 33384370]
30. Long G et al. Antianemia drug roxadustat (FG-4592) protects against doxorubicin-induced cardiotoxicity by targeting antiapoptotic and antioxidative pathways. Front. Pharm. 11, 1191 (2020).
31. Salnikow K et al. Depletion of intracellular ascorbate by the carcinogenic metals nickel and cobalt results in the induction of hypoxic stress. J. Biol. Chem. 279, 40337–40344 (2004). [PubMed: 15271983]
32. Wang GL & Semenza GL Desferrioxamine induces erythropoietin gene expression and hypoxia-inducible factor 1 DNA-binding activity: implications for models of hypoxia signal transduction. Blood 82, 3610–3615 (1993). [PubMed: 8260699]
33. Duan LJ, Takeda K & Fong GH Hematological, hepatic, and retinal phenotypes in mice deficient for prolyl hydroxylase domain proteins in the liver. Am. J. Pathol. 184, 1240–1250 (2014). [PubMed: 24508125]
34. Samson AL et al. A toolbox for imaging RIPK1, RIPK3, and MLKL in mouse and human cells. Cell Death Differ. 28, 2126–2144 (2021). [PubMed: 33589776]
35. Xie T et al. Structural basis of RIP1 inhibition by necrostatins. Structure 21, 493–499 (2013). [PubMed: 23473668]
36. Zheng X et al. Prolyl hydroxylation by EglN2 destabilizes FOXO3a by blocking its interaction with the USP9x deubiquitinase. Genes Dev. 28, 1429–1444 (2014). [PubMed: 24990963]
37. Zhu K et al. Necroptosis promotes cell-autonomous activation of proinflammatory cytokine gene expression. Cell Death Dis. 9, 500 (2018). [PubMed: 29703889]
38. Jaakkola P et al. Targeting of HIF-α to the von Hippel–Lindau ubiquitylation complex by O_2-regulated prolyl hydroxylation. Science 292, 468–472 (2001). [PubMed: 11292861]
39. Ivan M et al. HIFα targeted for VHL-mediated destruction by proline hydroxylation: implications for O_2 sensing. Science 292, 464–468 (2001). [PubMed: 11292862]
40. Yu F, White SB, Zhao Q & Lee FS HIF-1α binding to VHL is regulated by stimulus-sensitive proline hydroxylation. Proc. Natl Acad. Sci. USA 98, 9630–9635 (2001). [PubMed: 11504942]
41. Chen Z et al. Crucial role of p53-dependent cellular senescence in suppression of Pten-deficient tumorigenesis. Nature 436, 725–730 (2005). [PubMed: 16079851]
42. Min JH et al. Structure of an HIF-1α–pVHL complex: hydroxyproline recognition in signaling. Science 296, 1886–1889 (2002). [PubMed: 12004076]
43. Hon WC et al. Structural basis for the recognition of hydroxyproline in HIF-1α by pVHL. Nature 417, 975–978 (2002). [PubMed: 12050673]
44. Roe JS et al. p53 stabilization and transactivation by a von Hippel–Lindau protein. Mol. Cell 22, 395–405 (2006). [PubMed: 16678111]
45. Rankin EB et al. Hypoxia-inducible factor 2 regulates hepatic lipid metabolism. Mol. Cell. Biol. 29, 4527–4538 (2009). [PubMed: 19528226]
46. Krishna-Subramanian S et al. RIPK1 and death receptor signaling drive biliary damage and early liver tumorigenesis in mice with chronic hepatobiliary injury. Cell Death Differ. 26, 2710–2726 (2019). [PubMed: 30988397]
47. Dara L, Liu ZX & Kaplowitz N Questions and controversies: the role of necroptosis in liver disease. Cell Death Discov. 2, 16089 (2016). [PubMed: 27924226]

48. Masson N, Willam C, Maxwell PH, Pugh CW & Ratcliffe PJ Independent function of two destruction domains in hypoxia-inducible factor-α chains activated by prolyl hydroxylation. EMBO J. 20, 5197–5206 (2001). [PubMed: 11566883]

49. Eltzschig HK & Carmeliet P Hypoxia and inflammation. N. Engl. J. Med. 364, 656–665 (2011). [PubMed: 21323543]

50. Yuan X et al. Targeting hypoxia signaling for perioperative organ injury. Anesth. Analg. 126, 308–321 (2018). [PubMed: 28759485]

51. Rosenberger P et al. Hypoxia-inducible factor-dependent induction of netrin-1 dampens inflammation caused by hypoxia. Nat. Immunol. 10, 195–202 (2009). [PubMed: 19122655]

52. Guo J et al. pVHL suppresses kinase activity of Akt in a proline-hydroxylation-dependent manner. Science 353, 929–932 (2016). [PubMed: 27563096]

53. Chowdhury R et al. Structural basis for binding of hypoxia-inducible factor to the oxygen-sensing prolyl hydroxylases. Structure 17, 981–989 (2009). [PubMed: 19604478]

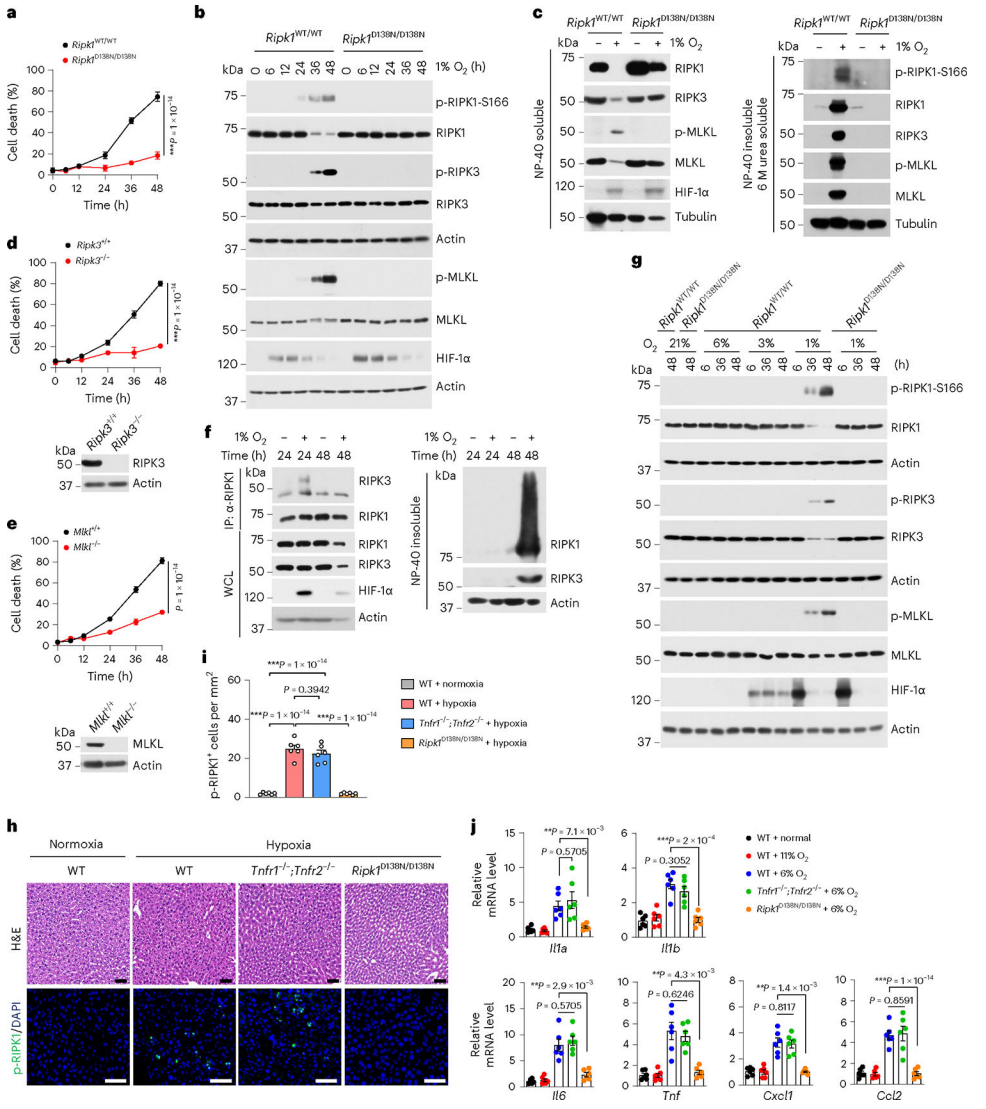

Fig. 1 |. Hypoxia induces cell death in a RIPK1-dependent manner.

a–**c**, MEFs of the indicated genotypes were exposed to 1% O_2 for the indicated times. **a**, Cell death was measured by propidium iodide uptake assay. The data represent means ± s.d. of $n = 3$ biologically independent samples. **b**,**c**, Levels of p-RIPK1-S166 and p-MLKL(S345) under 1% O_2 at the indicated times (**b**) and with or without 1% O_2 at 48 h (**c**), as determined by immunoblotting. The results are representative of three independent experiments. In **c**, the blots derived from a single membrane were grouped together. **d**,**e**, Top, WT and either *Ripk3* knockout MEFs (**d**) or *Mlkl* knockout MEFs (**e**) were exposed to 1% O_2 for the indicated times and cell death was measured by propidium iodide uptake assay. The data represent means ± s.d. of $n = 3$ biological independent samples. Bottom, the cell lines were validated with immunoblotting. **f**, MEFs were exposed to 1% O_2 for the indicated times. Whole cell lysates (WCL) were immunoprecipitated with anti-RIPK1 antibody and the immunocomplexes were analysed by immunoblotting using anti-RIPK3 antibody. The results are representative of three independent experiments. **g**, MEFs of the indicated genotypes were exposed to different oxygen concentrations for the indicated times.

The levels of p-RIPK1-S166 and p-MLKL-S345 were determined by immunoblotting. The results are representative of three independent experiments. **h**–**j**, WT, *Tnfr1/2* double knockout and *Rpik1*$^{D138N/D138N}$ mice were challenged with 6 or 11% O_2 for 72 h. **h**, Histological analysis and immunostaining for p-RIPK1-S166 on liver sections ($n = 6$). Nuclei were detected by DAPI staining. Scale bars, 100 μm. **i**, Microscopic quantification of p-RIPK1-S166-positive cells. **j**, Quantitative reverse transcription PCR analysis of the messenger RNA expression of the indicated cytokines and chemokines ($n = 6$). The data represent means ± s.e.m. Statistical significance was determined by one-way ANOVA with post-hoc Dunnett's test (**i** and **j**) or two-way ANOVA (**a**, **d** and **e**). H&E, haematoxylin and eosin.* $p<0.5$, ** $p<0.01$, *** $p<0.001$.

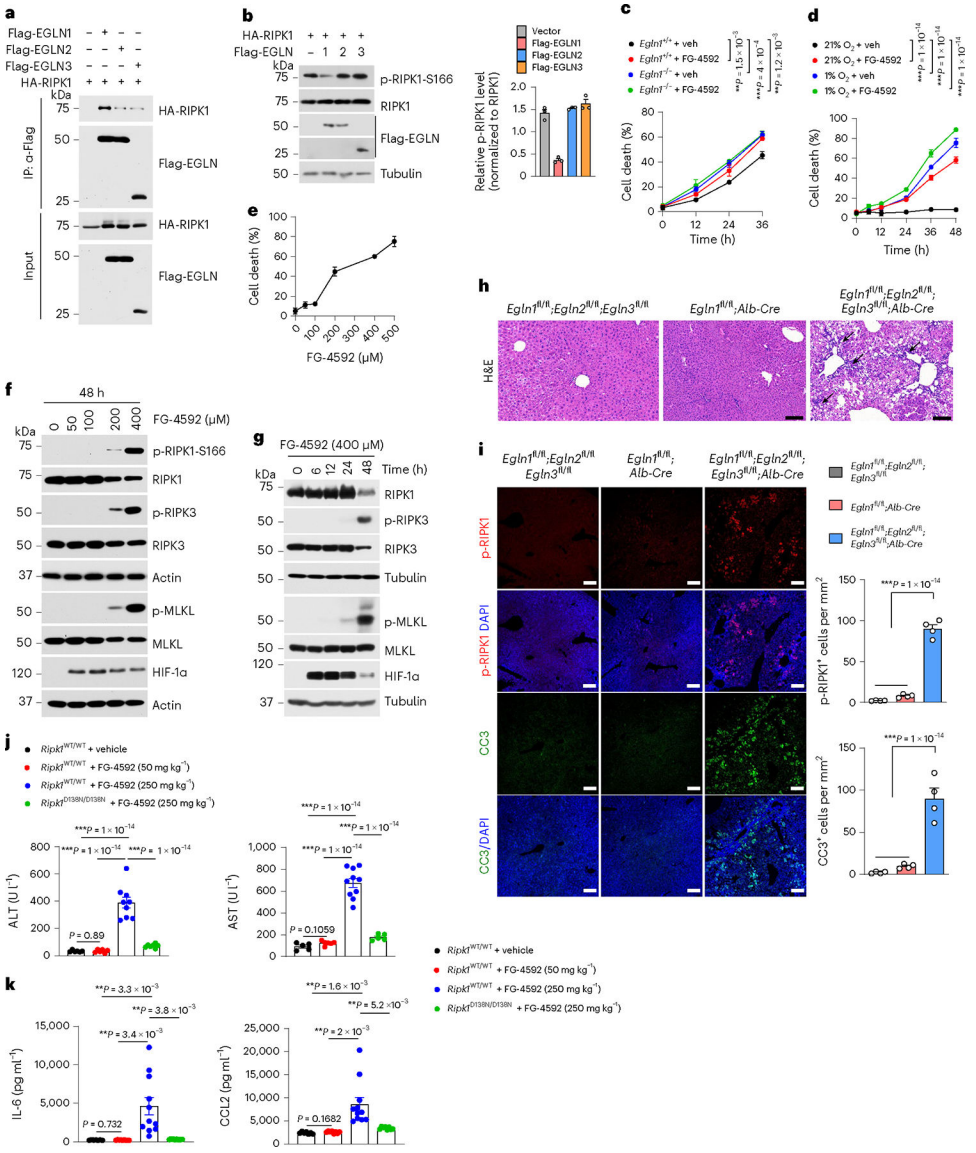

Fig. 2 |. Inhibition of EGLN1 promotes RIPK1 activation.

a,**b**, 293T cells were transfected with the indicated expression vectors. **a**, Cell lysates were immunoprecipitated with anti-Flag antibody and the immunocomplexes were analysed by immunoblotting using anti-HA antibody. The results are representative of three independent experiments. **b**, Left, levels of p-RIPK1-S166, as determined by immunoblotting. Right, ImageJ quantification of the data from three independent experiments. The data represent means ± s.e.m. of $n = 3$ independent experiments. **c**,**d**, *Egln1*$^{+/+}$ and *Egln1*$^{-/-}$ MEFs were exposed to 1% O_2 (**c**) and *Egln1*$^{+/+}$ MEFs were exposed to either 1 or 21% O_2 (**d**) with or without 200 μM FG-4592 for the indicated times and cell death was measured by propidium iodide uptake assay. The data represent means ± s.d. of $n = 3$ biologically independent samples. **e**–**g**, MEFs were treated with the indicated concentrations of FG-4592. **e**, Cell death was measured by propidium iodide uptake assay. The data represent means ± s.d. of $n = 3$ biologically independent samples. **f**,**g**, Levels of p-RIPK1-S166 and p-MLKL-S345 at the indicated concentrations of FG-4592 after 48 h (**f**) and at 400 μm FG-4592 at the

indicated times (**g**), as determined by immunoblotting. The results are representative of three independent experiments. **h**, Histological analysis of liver sections from the indicated genotypes. **i**, Left, immunostaining for p-RIPK1-S166 and CC3 at the age of 6 weeks ($n = 4$). Nuclei were detected by DAPI staining. Scale bars, 100 μm. Right, microscopic quantification of CC3- and p-RIPK1-S166-positive cells. The data represent means ± s.e.m. **j**, Serum ALT ($n = 6$ (*Ripk1*$^{WT/WT}$ + vehicle and *Ripk1*$^{WT/WT}$ + FG-4592 (50 mg kg^{-1})), 9 (*Ripk1*$^{WT/WT}$ + FG-4592 (250 mg kg^{-1})) or 7 (*Ripk1*$^{D138N/D138N}$ + FG-4592 (250 mg kg^{-1}))) and AST levels ($n = 5$ (*Ripk1*$^{WT/WT}$ + vehicle and *Ripk1*$^{D138N/D138N}$ + FG-4592 (250 mg kg^{-1})), 6 *Ripk1*$^{WT/WT}$ + FG-4592 (50 mg kg^{-1})) or 10 (*Ripk1*$^{WT/WT}$ + FG-4592 (250 mg kg^{-1}))). **k**, Enzyme-linked immunosorbent assay analyses of IL-6 ($n = 7$ (*Ripk1*$^{WT/WT}$ + vehicle), 9 (*Ripk1*$^{WT/WT}$ + FG-4592 (50 mg kg^{-1})), 11 (*Ripk1*$^{WT/WT}$ + FG-4592 (250 mg kg^{-1})) or 10 (*Ripk1*$^{D138N/D138N}$ + FG-4592 (250 mg kg^{-1}))) and CCL2 ($n = 7$ (*Ripk1*$^{WT/WT}$ + vehicle), 8 (*Ripk1*$^{WT/WT}$ + FG-4592 (50 mg kg^{-1}) and *Ripk1*$^{D138N/D138N}$ + FG-4592 (250 mg kg^{-1})) or 11 (*Ripk1*$^{WT/WT}$ + FG-4592 (250 mg kg^{-1}))). The data represent means ± s.e.m. Statistical significance was determined by two-way ANOVA with post-hoc Bonferroni's test (**c** and **d**) or one-way ANOVA with post-hoc Dunnett's test (**i**, **j** and **k**). IP, immunoprecipitate; veh, vehicle.

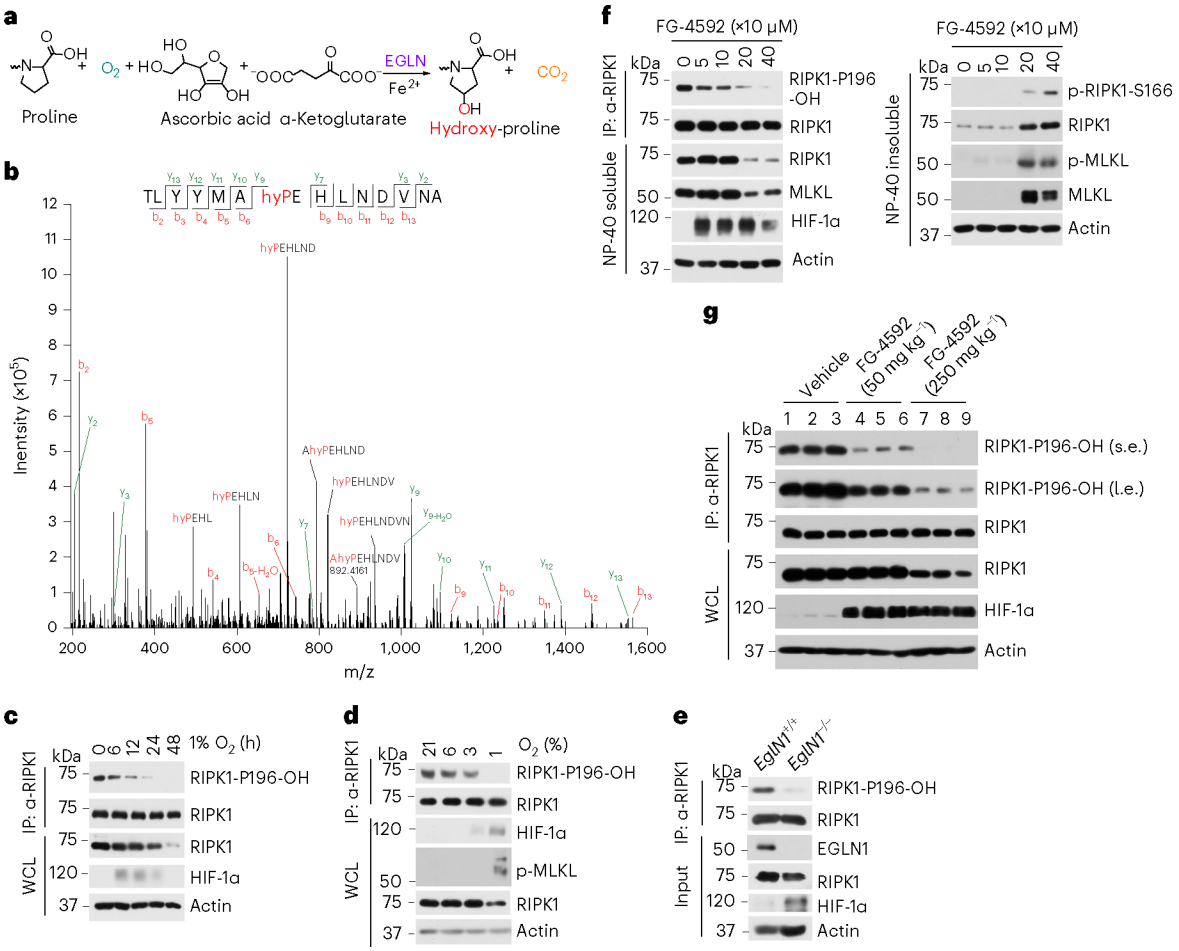

Fig. 3 |. EGLN1 regulates RIPK1 activation by hydroxylating RIPK1.

a,**b**, Mass spectrometry analysis (**b**) detected the presence of a proline hydroxylation event (the reaction and chemical structures are shown in **a**) at the RIPK1 Pro195 site in the reaction products of in vitro hydroxylation assays with recombinant His-EHLN1 and synthetic RIPK1 peptide spanning the Pro195 region. **c**–**f**, Cell lysates were immunoprecipitated with anti-RIPK1 antibody and the immunocomplexes were analysed by western blotting using anti-Pro196 hydroxylation antibody. **c**, MEFs exposed to 1% O_2 for the indicated times. **d**, MEFs exposed to the indicated concentrations of O_2 for 48 h. **e**, MEFs of the indicated genotypes. **f**, MEFs treated with the indicated concentrations of FG-4592 for 48 h. The results are representative of three independent experiments. **g**, Liver samples from 6- to 8-week-old WT mice ($n = 3$) were injected intraperitoneally with vehicle control or FG-4592 at a dose of 50 or 250 mg kg^{-1} body weight every 24 h for 2 d. The cell lysates were immunoprecipitated with anti-RIPK1 antibody and the immunocomplexes were analysed by immuno blotting using anti-Pro196 hydroxylation antibody. s.e., short exposure; l.e., long exposure.

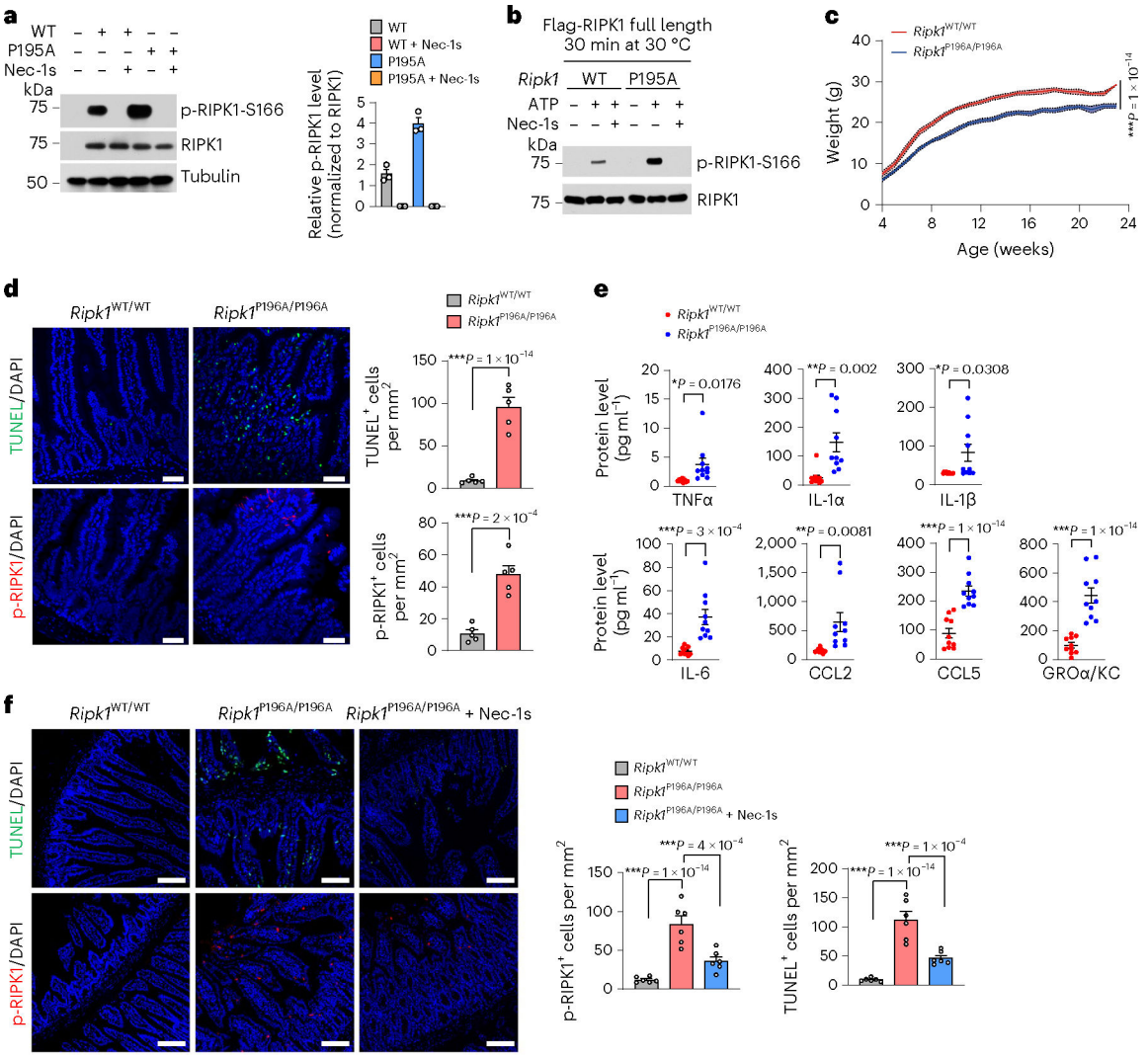

Fig. 4 |. RIPK1-P196A mutation promotes RIPK1 activation in mice.

a,**b**, 293T cells were transfected with expression vectors of Flag-tagged WT or mutant RIPK1. **a**, The levels of p-RIPK1-S166 were determined by immunoblotting. 10 μM Nec-1s was used. The data represent means ± s.e.m. of $n = 3$ independent experiments. **b**, Cells were treated with 10 μM Nec-1s at the same time for 20 h. Cell lysates were immunoprecipitated using anti-Flag beads and incubated with or without 100 μM ATP and 50 μM Nec-1s, as indicated, at 30 °C for 30 min. The samples were analysed by immunoblotting with p-RIPK1-S166. The results are representative of three independent experiments. **c**, Weight changes of male WT ($n = 20$) and *Ripk1*$^{P196A/P196A}$ mice ($n = 23$) at 4–22 weeks of age. The data represent means ± s.e.m. **d**, Left, TUNEL assays and immunostaining for p-RIPK1-S166 were performed on intestine sections from *Ripk1*$^{P196A/P196A}$ and control WT littermate mice ($n = 5$). Nuclei were detected by DAPI staining. Scale bars, 100 μm. Right, microscopic quantification of TUNEL- and p-RIPK1-S166-positive cells. The data represent means ± s.e.m. **e**, Luminex immunoassay analysis of the protein expression of the indicated cytokines and chemokines ($n = 10$). The data represent means ± s.e.m. **f**, Left, TUNEL assays and immunostaining for p-RIPK1-S166

were performed on intestine sections from the indicated genotypes with or without treatment with Nec-1s for 7 d ($n = 6$). Nuclei were detected by DAPI staining. Right, microscopic quantification of TUNEL- and p-RIPK1-S166-positive cells. The data represent means ± s.e.m. Statistical significance was determined by two-way ANOVA (**c**), unpaired two-tailed *t*-test (**d** and **e**) or one-way ANOVA with post-hoc Dunnett's test (**f**). GROα/KC, chemokine (C-X-C motif) ligand 1 (CXCL1).

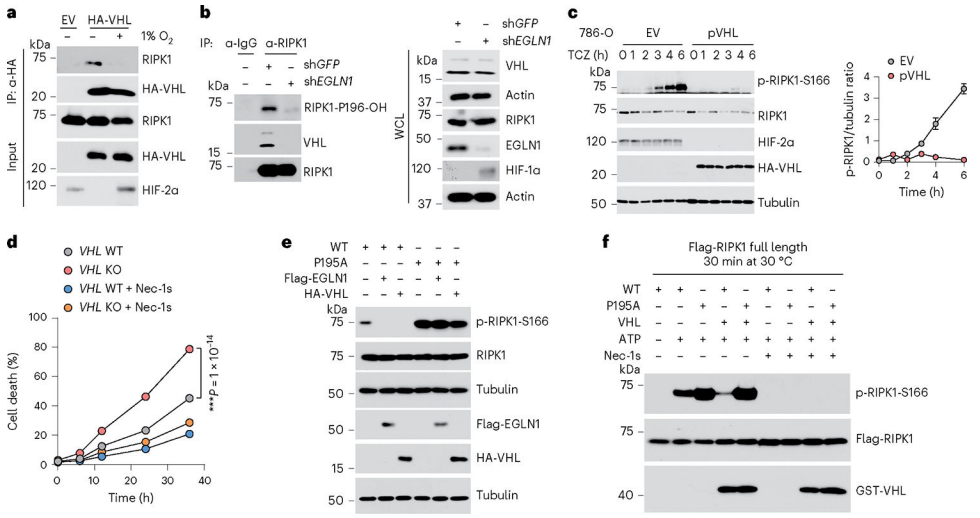

Fig. 5 |. pVHL suppresses RIPK1 activity by direct binding.

a, *VHL*-deficient SW839 cells were re-introduced with pVHL and then exposed to 1% O_2 for 24 h. Cell lysates were immunoprecipitated with anti-HA antibody and the immunocomplexes were analysed by western blotting using anti-RIPK1 antibody. The results are representative of three independent experiments. **b**, Cell lysates from control and *EGLN1* knockdown 293T cells were immunoprecipitated with anti-RIPK1 antibody and the immunocomplexes were analysed by immunoblotting using anti-Pro195 hydroxylation and VHL antibodies. The results are representative of three independent experiments. **c**, *VHL*-deficient 786-O cells were re-introduced with pVHL and then treated with TCZ (10 ng ml^{-1} TNFα, 2.5 μg ml^{-1} cycloheximide and 20 μM zVAD-fmk) for the indicated times. The levels of p-RIPK1-S166 were determined by immunoblotting. The data represent means ± s.e.m. of $n = 3$ independent experiments. **d**, WT or *Vhl* knockout MEFs were exposed to 1% O_2 in the presence or absence of 25 M Nec-1s. Cell death was measured by propidium iodide uptake assay. The data represent means ± s.d. of $n = 3$ biologically independent samples. Statistical significance was determined by two-way ANOVA. **e**, 293T cells were transfected with the indicated expression vectors for 24 h and the levels of p-RIPK1-S166 were determined by immunoblotting. The results are representative of three independent experiments. **f**, 293T cells were transfected with the indicated expression vectors and the cells were treated with 10 μM Nec-1s at the same time for 20 h. Cell lysates were immunoprecipitated using anti-Flag beads and incubated with or without 100 μM ATP, 50 μM Nec-1s or purified recombinant VHL, as indicated, at 30 °C for 30 min. The samples were analysed by immunoblotting with p-RIPK1-S166. The results are representative of two independent experiments. EV, empty vector; HA, Influenza hemagglutinin tag.

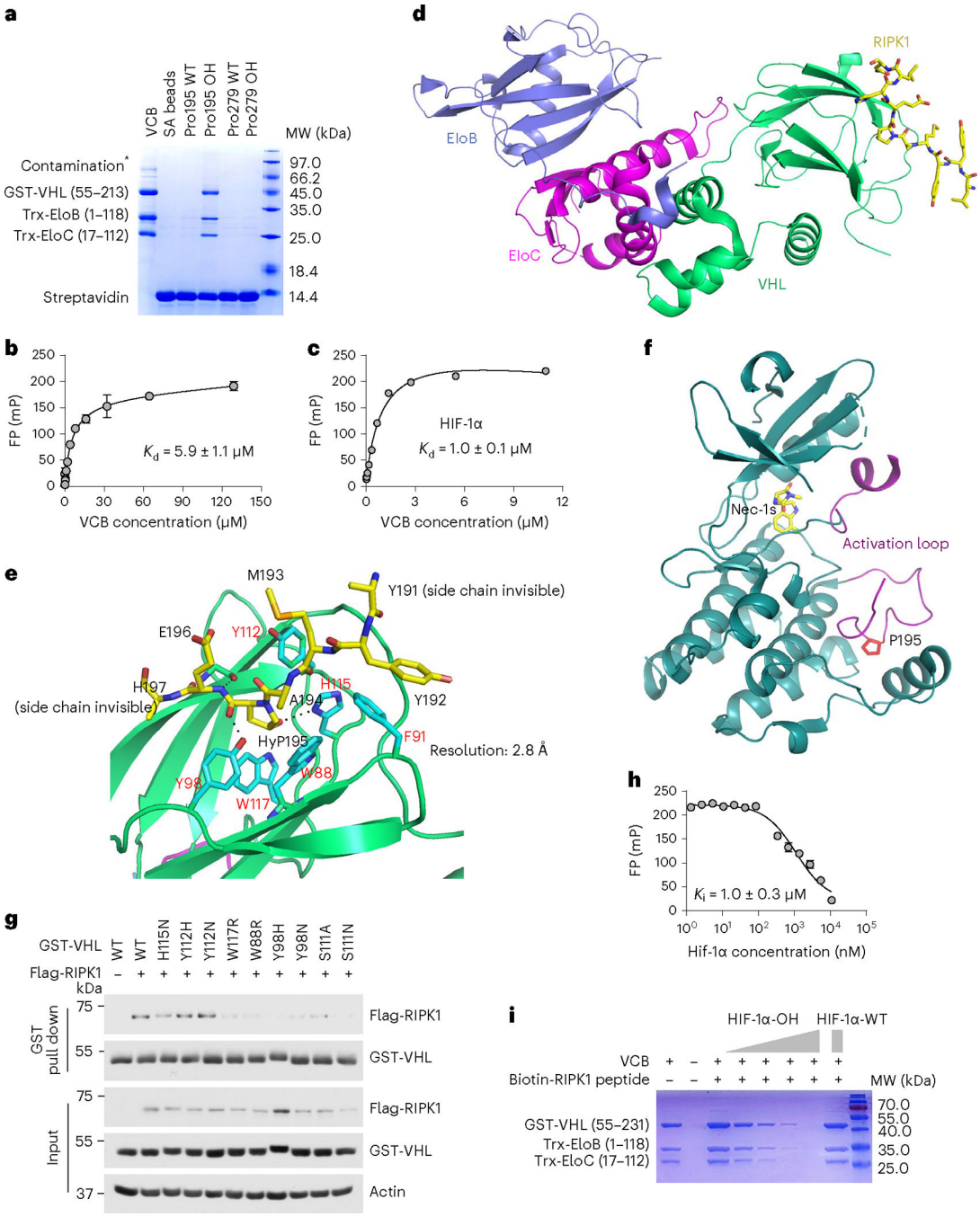

Fig. 6 |. Co-crystal structure of pVHL bound with hydroxylated RIPK1 peptide.

a, The direct binding between VCB and RIPK1 peptide was detected by pull-down assay. The results are representative of three independent experiments. Contamination* band indicates a band that is not a part of the purified VCB complex, but likely a contaminated non-specific protein. **b**,**c**, Dissociation constants (K_d) of the binding between recombinant VCB and either RIPK1 peptide (**b**) or HIF-1α peptide (**c**), as determined by fluorescence polarization (FP) assays. The data represent means ± s.d. of $n = 3$ biologically independent samples. **d**, VCB proteins in complex with a peptide of RIPK1 solved by

X-ray crystallography. **e**, Crucial residues in pVHL for the recognition of hydroxyproline in RIPK1 are shown as cyan sticks. RIPK1 peptides are shown as yellow sticks. Hydrogen bonds critical for pVHL–RIPK1 binding are shown as dashed lines. **f**, Crystal structure of the RIPK1 kinase domain complexed with the Nec-1s compound, showing the residue Pro195 (in stick form) localization in the activation loop (magenta) of the kinase domain (PDB ID: 4ITH)[35]. **g**, 293T cells were transfected with the indicated expression vectors. Cell lysates were immunoprecipitated with anti-GST antibody and the immunocomplexes were analysed by immunoblotting using anti-Flag antibody. The results are representative of three independent experiments. **h**, Fluorescein isothiocyanate-labelled RIPK1 peptide (500 nM) with VCB (5 μM) was mixed with increasing concentrations of HIF-1α peptide. The data represent means ± s.d. of $n = 3$ biologically independent samples. **i**, Streptavidin beads were charged with biotin-labelled RIPK1 peptide and incubated with VCB complex. Different concentrations (5, 10, 20 and 100 μM) of HIF-1α-OH peptide or 100 μM HIF-1α-WT peptide were added to incubate with the loaded beads for 1 h. The bound VCB proteins were resolved by SDS-PAGE. The results are representative of two independent experiments. EloB, elongin B; EloC, elongin C; MW, molecular weight. Ki, inhibition constant; SA, streptavidin.

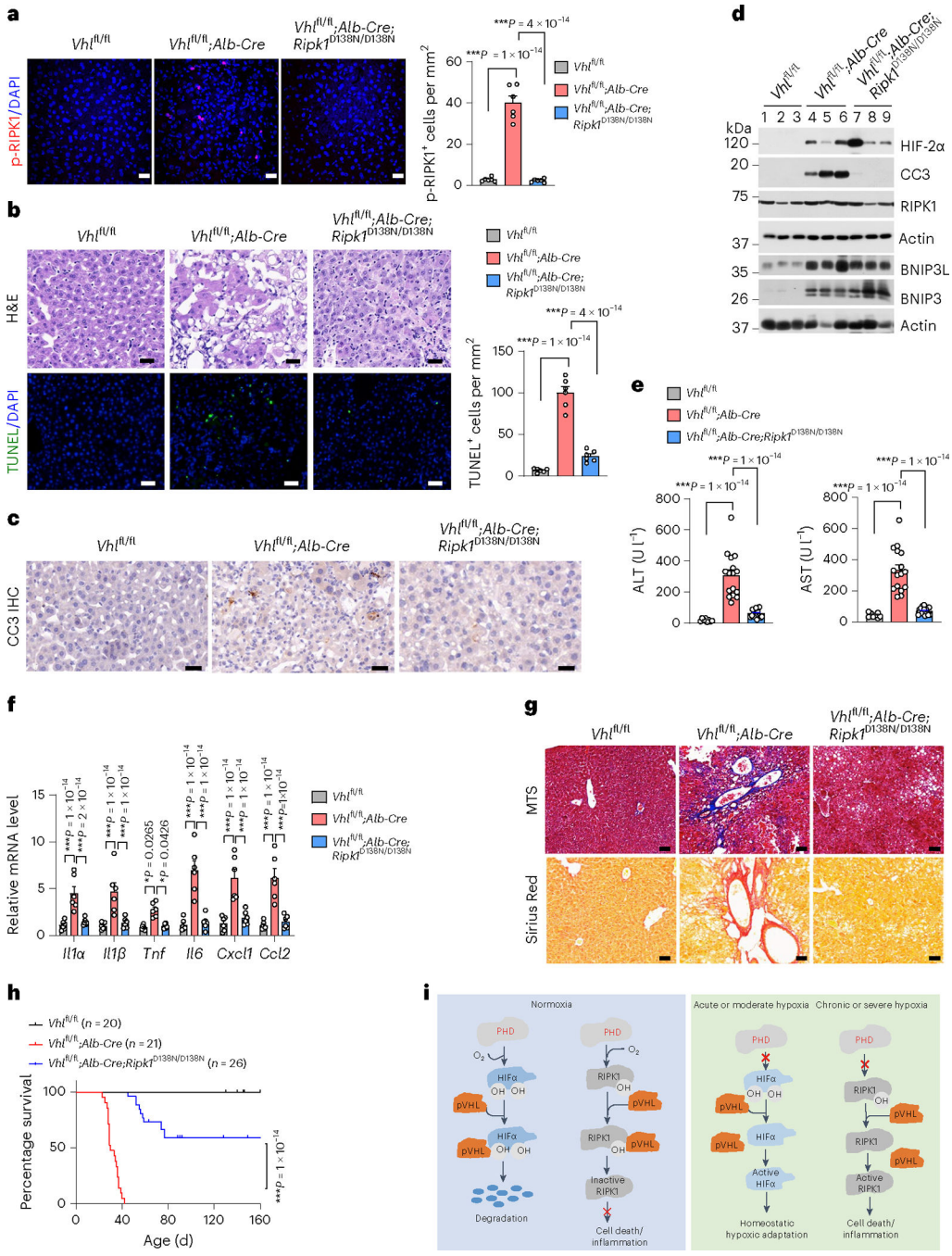

Fig. 7 |. Inhibition of RIPK1 suppresses inflammation induced by *Vhl* deletion.

a–**c**, Immunostaining for p-RIPK1-S166 (**a**), histological analysis and TUNEL assays (**b**) and CC3 staining (**c**) were performed on liver sections from *Vhl* LKO, *Vhl* LKO;*Ripk1*$^{D138N/D138N}$ and control WT littermate mice ($n = 6$). Nuclei were detected by DAPI staining. Scale bars, 100 μm. Right, quantification of p-RIPK1-S166- (**a**) and TUNEL-positive cells (**b**). The data are presented as means ± s.e.m. **d**, The liver extracts from *Vhl* LKO, *Vhl* LKO;*Ripk1*$^{D138N/D138N}$ and control WT littermate mice ($n = 3$) were analysed by immunoblotting with the indicated antibodies. **e**, Serum ALT and AST levels

were measured from WT (n = 8), *Vhl* LKO (n = 16) and *Vhl* LKO;*Ripk1*$^{D138N/D138N}$ (n = 16) mice. **f**, Quantitative reverse transcription PCR analysis of the messenger RNA expression of cytokines and chemokines in 4-week-old mouse livers from *Vhl* LKO, *Vhl* LKO;*Ripk1*$^{D138N/D138N}$ and control WT littermate mice (n = 6). The data are presented as means ± s.e.m. **g**, Representative images of Masson's trichrome (MTS) or Sirius Red staining on liver sections from mice of the indicated genotypes at the age of 4 weeks (n = 6). Scale bars, 100 μm. **h**, Kaplan–Meier survival curve plot for *Vhl* LKO, *Vhl* LKO;*Ripk1*$^{D138N/D138N}$ and control WT littermate mice. **i**, Schematic to better illustrate the conceptual advancement in our understanding of how cells respond to hypoxia. In mild or short-time exposure to hypoxia, cells stabilize HIF-1α as a pro-survival signal to better adapt to the hypoxic environment. However, in cases of severe hypoxia with prolonged treatment that leads to irreversible damage to cells or tissues, cells trigger RIPK1 activation, which is presumably maladaptive, to eliminate the damaged unrepairable cells. Cells switch from HIF-1α-dependent homeostatic hypoxic adaptation to RIPK1-dependent cell death and inflammation. Statistical significance was determined by one-way ANOVA with post-hoc Dunnett's test (**a**, **b**, **e** and **f**) or two-sided log-rank (Mantel–Cox) test (**h**). IHC, immunohistochemistry.